

Leveraging Cation Identity to Engineer Solid Electrolyte Interphases for Rechargeable Lithium Metal Anodes

Richard May,¹ Yumin Zhang,² Steven R. Denny,¹ Venkatasubramanian Viswanathan,^{2,3,*} Lauren E. Marbella^{1,*}

SUMMARY

Lithium metal anodes enable substantially higher energy density than current technologies for Li batteries. However, rechargeable Li metal anodes suffer from low Coulombic efficiency (loss of electrochemically active Li), leading to poor cycle life and safety. Engineering the electrolyte formulation to form a stable, well-functioning solid electrolyte interphase (SEI) is a promising approach to improving these performance figures of merit. While design rules have been established for selecting electrolyte solvents and salt anions to establish a more robust SEI, the impact of altering cation identity is not well understood. In this work, we demonstrate that alkali metal additives (here, K⁺) alter SEI composition and thickness. Through post-mortem elemental analyses, we show that K⁺ ions do not directly participate in metal electrodeposition, but rather modify the chemical and electrochemical reactivity of the electrode-electrolyte interface. Through a combination of quantitative nuclear magnetic resonance (NMR) spectroscopic characterization and density functional theory (DFT) simulations, we show that decomposition of electrolyte solvent molecules, ethylene carbonate (EC) and dimethyl carbonate (DMC), at the lithium metal surface is suppressed in the presence of a K⁺ additive. We attribute this to K⁺ being a softer cation compared to Li⁺, leading to preferred pair formation between K⁺ and the soft base carbonates, and thus increased salt-solvent coordination. Electrolyte cation engineering is an underexplored strategy to control the SEI, and we believe that the mechanistic understanding and insight developed in this work will spur further investigation of this promising approach.

KEYWORDS: lithium metal anode, solid electrolyte interphase, alkali metal additive, lithium microstructural growth, carbonate decomposition, electrolyte-electrode interface modeling

INTRODUCTION

The high specific energy of Li metal anodes is necessary for electrifying certain sectors of transportation and aviation.^{1,2} In addition, Li metal is required for many next-generation battery chemistries that offer improvements in energy density and safety such as Li-S (2600 Wh/kg),³ Li-air (13000 Wh/kg),^{4–6} and all solid-state batteries.^{7,8} Unfortunately, rechargeable Li metal anodes exhibit short-circuiting behavior that is associated with uneven Li plating and stripping which forms microstructural Li on the surface of the electrode.^{9,10} As a result, Li metal anodes face significant challenges in implementation due to serious safety concerns and a loss of Coulombic efficiency over the course of electrochemical cycling.¹¹

¹ Department of Chemical Engineering, Columbia University, New York, New York 10027, United States

² Department of Materials Science and Engineering, Carnegie Mellon University, Pittsburgh, Pennsylvania 15213, United States

³ Department of Mechanical Engineering, Carnegie Mellon University, Pittsburgh, Pennsylvania 15213, United States

* Correspondence: venkvis@cmu.edu, lem2221@columbia.edu

Numerous approaches have been proposed to enable stable plating of Li metal.^{12–17} Among these, altering the solid electrolyte interphase (SEI) that forms on the electrode surface is a simple and scalable approach that can readily produce low-surface area Li deposits and improved Coulombic efficiency in Li metal batteries.^{2,11,18–20} Widely used strategies to control the composition and thickness of the SEI include tailoring the anion of the Li salt,²¹ increasing the concentration of the electrolyte,^{22–26} and using sacrificial organic electrolyte additives.^{27–29} These strategies lead to increased amounts of LiF, cross-linking polymeric species, and polyene moieties in the SEI that are correlated with improved battery performance.^{12,27,30–34}

Conversely, the ramifications of altering cation identity are more complicated, as the cation (e.g. Li⁺) is electrochemically active and consumed to form various species in the SEI (e.g. Li₂CO₃, LiF). Previous reports have shown that the addition of alkali metal additives (e.g. K⁺, Cs⁺, Rb⁺) lead to smoother Li deposits and improved Coulombic efficiencies for Li metal when added to conventional Li battery electrolytes.^{35–37} The enhanced performance for Li metal in the presence of alkali metal additives has been attributed to electrostatic shielding,³⁵ thinning of the SEI,^{36,37} and changes in the relative ratios of different chemical species in the SEI.^{36,38} However, the eventual fate of the extrinsic alkali metal additive, as well as its role in electrochemical deposition and electrolyte decomposition, remains unclear.

Here, we report a quantitative assessment of both the thickness of the SEI and the extent of electrolyte decomposition during Li stripping/plating in the presence of K⁺ additives using solution and solid-state NMR (SSNMR) spectroscopy and correlate these results with Li deposition behavior observed in scanning electron microscopy (SEM). A robust analysis of the molecular structures present in the SEI that forms on Li metal using conventional 1D and 2D SSNMR is enabled for the first time using sample dilution strategies³⁹ and polarization transfer schemes. Upon addition of K⁺, the amount of polycarbonates and organofluorides in the SEI increases, which is concomitant with a decrease in the overall thickness of the SEI. When examined with energy dispersive X-ray spectroscopy (EDS) and atomic absorption spectroscopy (AAS), we find that K⁺ does not participate in electrochemical reaction. Rather, density functional theory (DFT) calculations, which are widely applied to study electrode/electrolyte interfacial chemistry,^{29,40} suggest that differences in ion-solvent coordination between K⁺ and Li⁺ are responsible for the observed changes in SEI composition and thickness, and may ultimately lead to the observed alterations in Li deposition morphology. Our findings suggest that tuning cation identity in the electrolyte salt may be a new route to optimize electrolyte formulations for rechargeable Li metal anodes.

RESULTS

K⁺ Additive Leads to Smooth Li Deposits and Reduced Microstructural Growth

Ex situ SEM was used to examine Li deposition behavior in the presence of various concentrations of KPF₆ additive to 1 M LiPF₆ in 1:1 EC:DMC (LP30) after galvanostatic polarization at 1 mA cm⁻² for 2 h. Figure 1 shows representative microstructural morphologies for electrolyte compositions with and without added KPF₆. Similar to previous literature reports,^{41,36,42} the conventional battery electrolyte, LP30, exhibits high surface area Li microstructures after plating (Figure 1a, f). Increasing the concentration of KPF₆ additive in the LP30 electrolyte from 0.10 M (Figure 1c, h) to 0.15 M (Figure 1e, j) results in a transition to increasingly more smooth, round Li microstructures that have a lower surface area. Additive concentrations of 0.25 M KPF₆ appear to revert back to high surface area microstructures, possibly due to solubility limitations observed for concentrations >0.25 M KPF₆ and show a loss of efficiency and greater electrolyte decomposition (Figures S2, S7, and S11, *vide infra*). Yet, these data suggest that small amounts of K⁺ additive (0.10–0.15 M) improve Li deposition behavior. To determine

whether this change in Li plating was due to the presence of the K^+ additive or a result of increased salt concentration, we also examined the Li morphologies formed in LP30 + 0.10 M LiPF₆ (Figure 1b, g). In both the LP30 and LP30 + LiPF₆ samples, high surface area Li deposits with thinner features are observed that are nearly indistinguishable between the two samples (Figures 1a and 1b, respectively). These data suggest Li microstructural morphology is influenced specifically by the addition of K^+ and not simply a result of increased electrolyte salt concentration.

Table 1 and Figure S17 describe Li microstructural thickness and the overall microstructural thickness distributions analyzed over multiple images and samples ($N = 2\text{--}3$). We observe that average microstructural thickness decreases as KPF₆ is added at concentrations >0.1 M (Table 1), with microstructural growth nearly halved for LP30 + 0.25 M KPF₆. (Unfortunately, solubility issues start to occur at this point, so LP30 + 0.25 M KPF₆ was not explored any further due to inconsistencies in the data). The improved Li plating behavior in the presence of KPF₆ additive also translates to an enhanced Coulombic efficiency (CE) in these cells. Addition of 0.1 M KPF₆ to LP30 results in an increase in CE from 84% for LP30 to 86% for LP30 + 0.1 M KPF₆ averaged over 100 cycles, while the average CE for LP30 + 0.25 M KPF₆ decreases to 81% (Figure S2). This suggests that reversibility of Li plating/stripping may be improved by addition of small amounts (ca. 0.1 M) of KPF₆, while larger quantities (0.25 M) of KPF₆ additive is detrimental to overall cell performance, possibly due to solubility issues noted above.

Table 1. Average Li microstructural thickness after galvanostatic polarization at 1 mA cm⁻² for 2 h.

| Electrolyte | Microstructural thickness (μm) |
|--------------------------------|--------------------------------|
| LP30 | 60 ± 10 μm |
| LP30 + 0.1 M LiPF ₆ | 56 ± 11 μm |
| LP30 + 0.1 M KPF ₆ | 61 ± 9 μm |
| LP30 + 0.15 M KPF ₆ | 42 ± 10 μm |
| LP30 + 0.25 M KPF ₆ | 36 ± 8 μm |

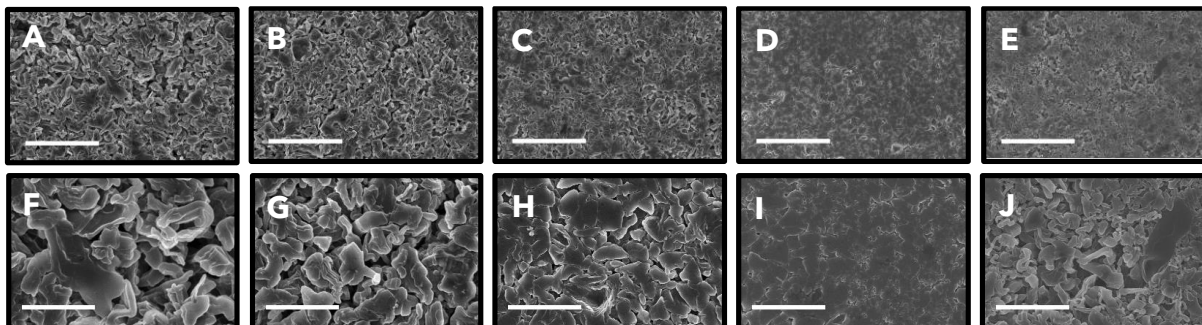


Figure 1. SEM data showing Li microstructural morphology at low magnification (A-E, top row, scale bar = 25 μm) and high magnification (F-J, bottom row, scale bar = 7.5 μm) for A, F) LP30 electrolyte, B, G) LP30 + 0.1 M LiPF₆, C, H) LP30 + 0.1 M KPF₆, D, I) LP30 + 0.15 M KPF₆, E, J) LP30 + 0.25 M KPF₆ after galvanostatic polarization at 1 mA cm⁻² for 2 h.

A Thinner, More Stable SEI in the Presence of K⁺

In order to understand the relationship between increased KPF₆ additive concentration and altered Li deposition, we examined the composition of the electrolyte post-cycling with solution NMR spectroscopy. Figure 2 shows ¹³C NMR of the Li electrolyte with and without added KPF₆ after extended cycling (94 cycles, earlier time points are shown in Figure S7). The major decomposition products present in both LP30 and LP30 + KPF₆ are methyl carbonate salts⁴³ and ethyl methyl carbonate.⁴⁴ Lithium methyl carbonate and/or potassium methyl carbonate (LMC/KMC) exhibit a ¹H shift at 3.27 ppm (s) and ¹³C shifts of 51 (Figure 2b, ε) and 156.5 ppm (Figure 2b, α). EMC shows ¹H resonances at 1.20 (t, $J_{HH} = 7.1$ Hz), 3.69 ppm (s), and 4.11 ppm (q, $J_{HH} = 7.1$ Hz) as well as ¹³C shifts at 14.1, 54.7, 63.6, and 155.6 ppm

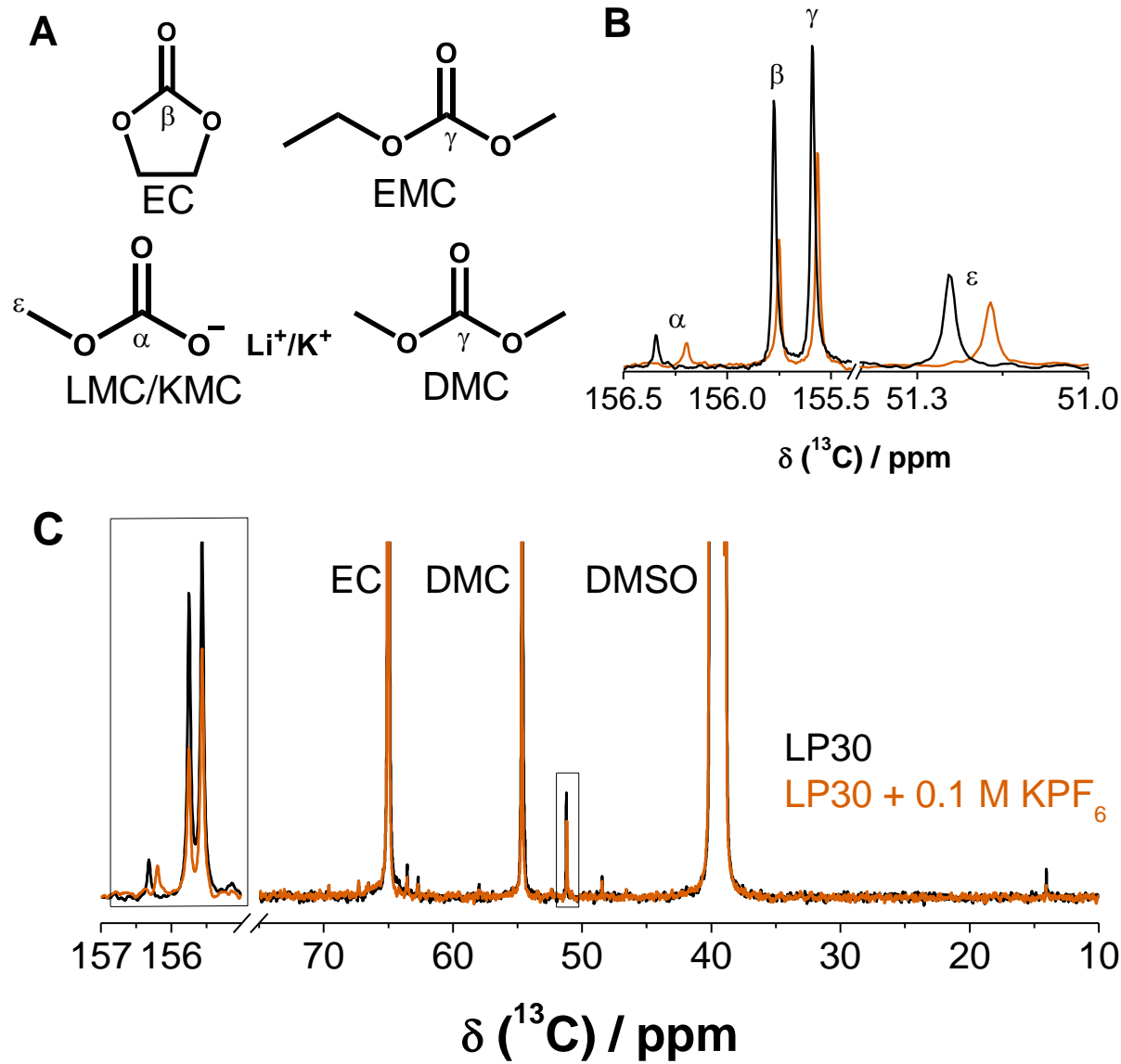


Figure 2. A) Electrolyte decomposition products assigned from B-C solution ¹³C NMR of LP30 (black) and LP30 + 0.1 M KPF₆ (orange) after 94 cycles at 1 mA/cm² for 2 h cycles. B) Carbonyl peaks for EC (β), DMC (γ), LMC (α), and EMC (γ), and methyl peaks for LMC (ε). C) Full ¹³C spectrum for both LP30 and LP30 + 0.1 M KPF₆. Solvent peaks EC, DMC, and DMSO-d₆ are cut off to highlight peaks due to electrolyte decomposition. Complete peak assignments are found in Table S1.

(Figure 2b, γ). Heteronuclear single-quantum correlation (HSQC) and multiple-bond (HMBC) ^1H - ^{13}C correlation experiments (Figure S3) were used to aid in assignment of LMC and EMC. HSQC cross peaks between $\delta(^1\text{H}) = 3.27$ ppm and $\delta(^{13}\text{C}) = 51$ ppm, as well as $\delta(^1\text{H}) = 4.12$ ppm and $\delta(^{13}\text{C}) = 63$ ppm, were used to assign LMC and EMC, respectively. An HMBC cross peak between $\delta(^1\text{H}) = 3.27$ ppm and $\delta(^{13}\text{C}) = 157$ ppm was used to assign LMC/KMC, yet overlapping peaks between DMC and EMC prevent definitive assignment of EMC using multiple-bond correlation experiments. Using solution NMR to analyze electrolyte decomposition products for varying KPF_6 additive concentrations (0, 0.1, 0.25 M KPF_6), we find that the position of the LMC/KMC ^1H peak shifts to higher frequencies at higher KPF_6 concentrations ($\delta(^1\text{H}) = 3.27$ ppm for 0 M KPF_6 , 3.29 ppm for 0.1 M KPF_6 , and 3.30 ppm for 0.25 M KPF_6), suggesting that more KMC (or free K^+ in the electrolyte) is present at higher KPF_6 additive concentrations (Figure S7). Minor amounts (<8%) of PEO-type oligomers are observed in ^1H (resonances at 3.56–3.57 and 3.61–3.63 ppm⁴⁵) and ^{13}C NMR (resonances at approximately 69 and 67 ppm) for all electrolyte solutions (Figure S7c). Quantitative comparison of ^1H NMR spectra indicate that $59 \pm 11\%$ more LMC and $52 \pm 9\%$ more EMC was observed for LP30 samples than LP30 + 0.1 M KPF_6 ($N = 2$). Therefore, while both electrolytes exhibit similar decomposition products, cells containing KPF_6 appear to show less organic decomposition and possibly, a more stable (i.e. less soluble) organic outer layer of the SEI.

Next, the insoluble components of the SEI were characterized with SSNMR spectroscopy. We note that prior to analysis, differences in microstructure quantity and sample conductivity were observed for LP30 versus LP30 + KPF_6 samples. Less Li microstructures were harvested from Li metal anodes containing KPF_6 for analysis, consistent with observations of reduced microstructural growth detected with SEM (*vide supra*). Further, when normalizing for sample mass, different sample dilutions in KBr were required to mitigate sample conductivity and allow MAS for LP30 compared to LP30 + KPF_6 . For the LP30 cells, Li microstructures were diluted 5:1 KBr :Li metal w/w and the samples easily spun to MAS = 27 kHz. At a dilution factor of 5:1 KBr :Li metal, samples containing KPF_6 additive were not able to spin at any frequency when the NMR probe was inserted into the magnet. Upon removal from the magnet, the sample readily spun to MAS = 12 kHz. However, attempts to slowly insert the probe inside the magnetic field while spinning resulted in a large decrease in MAS frequency, consistent with braking

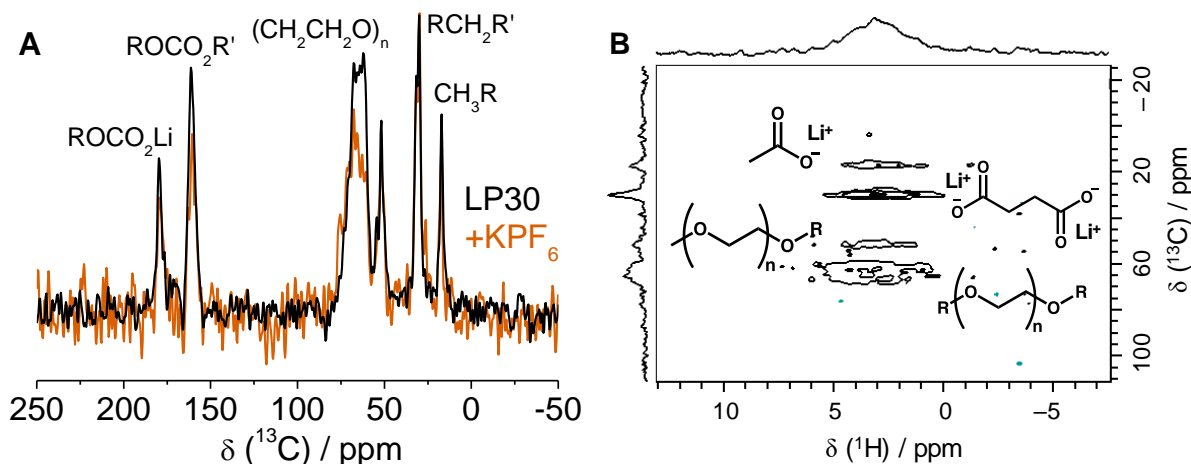


Figure 3. A) Solid-state CPMAS ^{13}C NMR (MAS = 18 kHz) and B) 2D ^1H -detected ^1H - ^{13}C HETCOR spectrum (MAS = 27 kHz) of electrolyte decomposition products for LP30 (black) and LP30 + 0.1 M KPF_6 (orange) after 94 cycles. Major decomposition products include polycarbonate and PEO-type species, as well as Li acetate and Li succinate. Both spectra were collected at room temperature.

from eddy currents produced by conductive/metallic samples.⁴⁶ Once samples containing KPF₆ were diluted to 10:1 KBr:Li metal, they were able to spin to MAS = 18 kHz, but could not go any faster. This difference in spinning behavior suggests that despite a similar dilution factor, Li microstructures formed from electrolytes containing KPF₆ additive contain more metallic Li and less SEI compared to LP30 samples. Conversely, these observations are consistent with microstructures from LP30 exhibiting thicker SEI layers (and thus, less overall Li metal), more readily enabling MAS by dilution from the SEI itself as well as the KBr.

Characterization with ¹H-¹³C CPMAS SSNMR shows characteristic SEI species, consistent with those that have been observed on the surface of Si and graphitic anodes when cycled in LP30.^{45,47} In the C=O region of the spectra, there are two peaks, one at 161 ppm, corresponding to polycarbonate moieties and one at 180 ppm corresponding to Li carboxylates (Figure 3a). The broad peaks centered at approximately 68 ppm are consistent with PEO-type polymers in the SEI, with some containing a methyl ether terminal group (¹³C shift at ~59 ppm). Further analysis with ¹H-detected ¹H-¹³C HETCOR confirm our assignment of PEO-type fragments and methyl ether terminal groups in the polymeric SEI (Figure 3b). The ¹³C resonances at ~32 ppm and ~19 ppm are consistent with CH₂ and CH₃ groups, respectively. We assign the ¹³C resonance at 32 ppm to Li succinate based on the position of the corresponding ¹H resonance (~3.0 ppm) and the ¹³C resonance at 19 ppm to Li acetate (¹H shift at ~2.7 ppm). Quantification of the ¹H-¹³C CPMAS SSNMR spectra indicates an approximately 20% decrease in overall SEI content upon addition of 0.1 M KPF₆ (¹³C intensities in Figure 3a have been adjusted based on sample mass to quantitatively represent the relative amounts of decomposition products present in electrolytes with (orange) and without (black) added KPF₆). It is worth noting that some sample-to-sample variation was observed in the species detected in the solid SEI. While PEO-type polymers and polycarbonate moieties were observed in all replicate samples, ¹³C resonances corresponding to Li carboxylates ($\delta(^{13}\text{C}) = 180$ ppm), Li succinate ($\delta(^{13}\text{C}) = 32$ ppm), and Li acetate ($\delta(^{13}\text{C}) = 19$ ppm) were prominently observed in the spectra shown in Figure 3, but were present in smaller quantities (e.g. Li succinate) or below the detection limit of SSNMR in other cells (Figure S8 and S11). The same trend is observed after 50 cycles (Figure S11) where 0.1 M KPF₆ additive consistently shows the lowest amount of SEI products. In other words, although the relative amounts of discrete species in the SEI was slightly different for individual cells, the trend of less SEI formation upon 0.1 M KPF₆ addition remained consistent. Less SEI on the surface of cells cycled with KPF₆ additive is also consistent with our observations from solution NMR spectroscopy as well as the differences observed in sample conductivity.

To accurately quantify the relative ratios of carbon-containing components in the SEI, we cycled Li/Li symmetric cells in 25% v/v ¹³C-enriched electrolytes to enable ¹³C direct polarization SSNMR experiments (Figure S8). Quantification of direct polarization spectra indicates that KPF₆-containing electrolyte is enriched in polycarbonate moieties (~161 ppm) and depleted in PEO fragments (~68 ppm). Prior work has suggested that polycarbonate species in the SEI may improve Li⁺ conductivity and lower SEI resistance.⁴⁸ In addition, direct polarization experiments show that LP30 decomposition results in the formation of nonconductive lithium carbonate (Li₂CO₃, 169 ppm,⁴⁹ ~10⁻⁸ S/cm⁵⁰), whereas this resonance is absent in KPF₆-containing electrolytes (or below the detection limit of the experiment).

K⁺-Solvent Ion Pair Formation Suppresses Electrolyte Decomposition

To understand how K⁺ additives alter electrolyte decomposition and the resulting SEI on Li metal, we used DFT calculations to examine how both EC- and DMC-Li surface interactions are influenced by KPF₆. Li{100} was selected due to its high surface stability.⁵¹ Simulations including LiPF₆ as a control were also investigated to highlight the difference between the LiPF₆ present in conventional electrolytes and the KPF₆ added to our electrolytes. Based on DFT optimized geometries, we measure and compare

the atomic bond distances formed between the atoms of electrolytes, alkali salts and the Li surface as an indicator of the extent of chemical reaction. This is further extended by exploring the charge transfer from the Li surface to the electrolyte and salt molecules using Bader analysis, which has previously been used to demonstrate correlations between charge transfer and chemical reactivity at the electrode-electrolyte interface.^{40,52}

The top row in Figure 4 shows the molecular structures of the electrolyte in the simulated systems. The second and third rows represent the final optimized atomic geometries from the DFT simulation, showing a top view (second row) and a side view (third row). Figure 4a shows adsorption of KPF₆ on Li{100} by gaining 0.44e⁻ from one of the Li atoms on the surface through two of the six F-functional groups. Comparing the initial and the optimized geometries, we see that the K⁺ ion within KPF₆ is slightly repelled by the Li surface, which can be rationalized by the Li-K binary phase diagram,⁵³ where no stable compounds or solid solutions are observed under 63.7 °C. Repulsion between K⁺ and Li{100} in our simulations and the known binary phase diagram both suggest a weak chemical interaction between Li and K and indicate that co-electrodeposition is unlikely. Conversely, Figure 4b shows LiPF₆ is adsorbed on the Li surface through two of the F-functional groups and two Li atoms on the surface, accompanied by approximately 4 times the charge transfer (1.60e⁻) as compared to the system involving

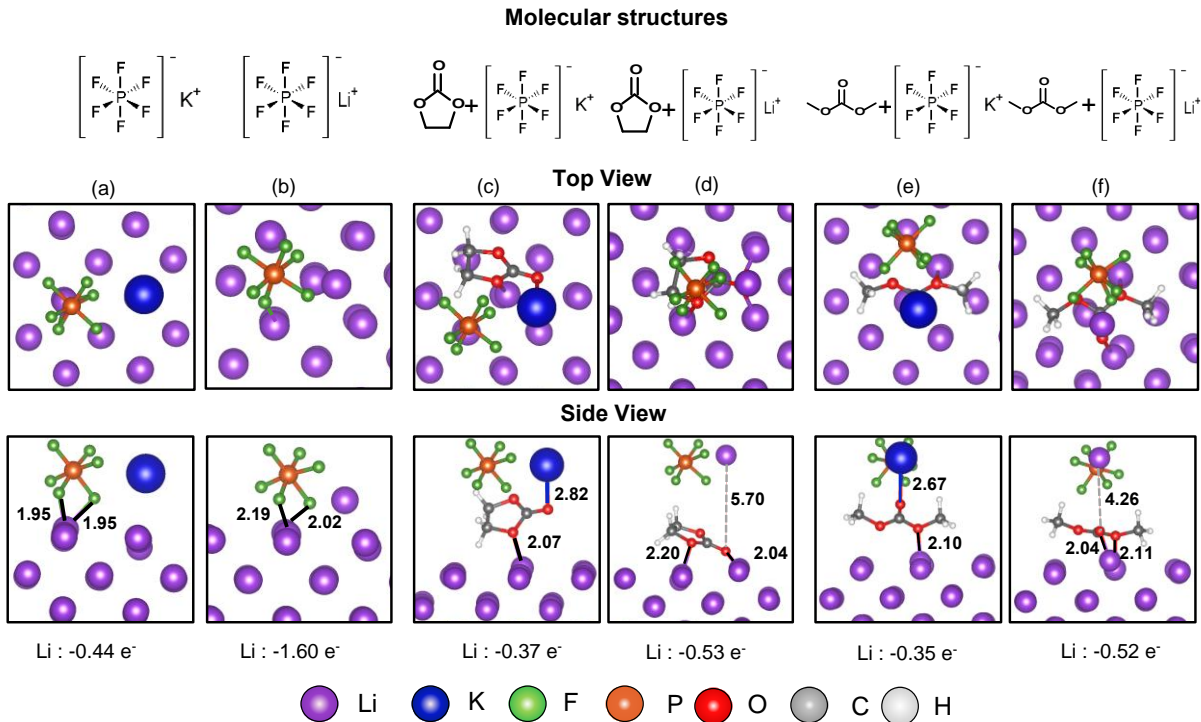


Figure 4. DFT simulations probing the reactivity of the Li metal-electrolyte interface in the presence of LiPF₆ and KPF₆. The first row shows a molecular representation of the electrolyte systems used in the simulation. The second row shows the top view and third row shows the side view of the DFT optimized geometries of A) KPF₆ + Li surface, B) LiPF₆ + Li surface, C) KPF₆ + EC + Li surface, D) LiPF₆ + EC + Li surface, E) KPF₆ + DMC + Li surface and F) LiPF₆ + DMC + Li surface. The bond distances in Å are included in each subfigure with the bonds formed between the solvent molecules and the Li surface shown in black, and the bonds representing solvent-salt coordination and incoordination shown in blue and dotted grey lines respectively. The charge transferred from the Li surface in each simulated system is marked underneath the side view. The key finding is that the carbonate electrolyte solvents preferably coordinate with KPF₆ rather than the Li surface, while the opposite case is observed when LiPF₆ is present.

KPF₆. Calculated charge transfer between the Li surface and electrolyte solvents serves as a proxy for consumption of active Li in side reactions. This reduced charge transfer in the presence of KPF₆ is correlated with chemical reactivity and indicates that the addition of K⁺ may limit the consumption of available Li during electrochemical cycling, which is consistent with our Coulombic efficiency measurements.

Figure 4c and 4e show the final optimized geometries of electrolyte systems that include KPF₆, the Li surface, and an electrolyte solvent molecule, EC or DMC, respectively. For both EC and DMC, we observe similar interaction mechanisms, where the carbonyl oxygen of the electrolyte molecule preferably coordinates with K⁺ in KPF₆ by forming an ion pair. The resulting oxygen-K⁺ bond distances are 2.82 Å and 2.67 Å for EC and DMC, respectively. Both of these bond lengths are close to 2.70 Å, which is the average bond length in K-O ionic crystals widely used in literature.⁵⁴ In addition, one of the surface Li atoms is weakly bonded to the singly bonded oxygen (-O-) in the carbonate group with 0.37e⁻ transferred from the Li surface to EC, and 0.35e⁻ transferred to DMC. The bonds formed with the surface show chemisorption character since the bond lengths (2.07 Å for EC and 2.10 Å for DMC) are similar to Li-O coordination (1.96 Å to 2.16 Å) in lithium oxide crystals⁵⁵ but far less than the van der Waals radii of Li and O combined (3.34 Å)⁵⁶, excluding a physisorption mechanism. Electron density distributions indicate that the bonds observed in electrolyte-salt and electrolyte-surface interactions are found at electron dense functional groups and are consistent with chemisorption (Figure S16).

In the presence of LiPF₆ (Figure 4d and 4f), both EC and DMC are chemisorbed on the Li surface through a bi-dentate interaction compared to mono-dentate in the case of KPF₆. For LiPF₆, the two bonds formed are between the carbonyl oxygen, the ethereal oxygen, and Li. Therein, one of these bonds is shorter (2.04 Å for both EC and DMC) than those found in the KPF₆ case, indicating that EC and DMC bind more strongly to the Li surface when only LiPF₆ is present. The second Li-O bond is a weak interaction (2.20 Å for EC and 2.11 Å for DMC), but provides additional coordination of the solvent molecule to the Li metal surface. The charge transfers from the Li surface (0.53e⁻ and 0.52e⁻ for EC and DMC respectively) to the solvent molecules are 1.4 times larger than in the systems involving KPF₆ as the alkali salt component. The atomic distances between Li⁺ in LiPF₆ and the carbonyl oxygens of EC and DMC are 5.70 Å and 4.26 Å respectively, excluding significant ion-solvent interaction. Conversely, the stronger electrostatic solvent-salt interaction in the presence of K⁺ (2.82 Å for EC and 2.62 Å for DMC) likely suppresses the adsorption of the carbonate electrolyte onto the Li surface and may ultimately mitigate electrolyte decomposition and form a thinner SEI.

Based on our DFT results, we hypothesize that the role of K⁺ additives is to mediate electrolyte decomposition in these electrolytes and that it does not participate in the electrochemical reaction (e.g. K⁺ is not deposited or stripped from the electrode surface during galvanostatic cycling, nor is K⁺ plated during polarization experiments). This hypothesis is supported by EDS measurements, which indicate that K is not deposited on the electrode surface after galvanostatic cycling (Figures S14 and S15). Analysis of battery electrolytes after different stages of cycling (1, 20, 50 and 93 cycles, Table S2) with AAS shows that while a small amount of K⁺ is consumed (~0.01 M) in the first cycle, the concentration of K⁺ in the electrolyte remains constant. The combination of DFT, EDS, and AAS provide compelling evidence that K⁺ is not electrochemically active in these formulations and instead, alters electrolyte-Li interfacial interactions and subsequent decomposition pathways.

DISCUSSION

Based on the experimental and theoretical data presented, we show that altering cation identity via the use of alkali metal additives in electrolyte formulations can lead to differences in Li deposition behavior that is correlated with changes in SEI stability and thickness. DFT calculations suggest that these alterations in electrolyte decomposition are likely the result of different alkali metal-electrolyte adsorption events between K⁺ and Li⁺ at the electrolyte-electrode interface. These data are consistent with other reports that suggest alkali metal additives reduce electrolyte consumption and improve Li plating morphologies, emphasizing the need for additional insight into alkali metal-mediated electrolyte decomposition.

In prior work, Mullins and coworkers soaked Li metal for 48 h in electrolyte baths both with and without KPF₆ additive and used XPS to show both an enrichment in C=O species and a depletion of PEO-containing compounds in the K⁺-mediated SEI.³⁶ They found that the initial SEI produced in the presence of K⁺ is enriched in LiF and depleted in other F-containing species. In contrast, ¹⁹F SSNMR measurements performed on our electrodes after extended cycling show that KPF₆ addition results in enrichment of other F-containing species (e.g. organofluorides), but the amount of LiF remains either unchanged (Figure S9) or decreases (Figure S10). In separate work, Meng and coworkers showed both a decrease in the amount of LiF and an increase in the amount of Li fluorophosphates in the SEI on Li metal when Cs⁺ additives were present using a combination of cryo-EM and XPS.³⁷ Given the discrepancies surrounding the role of LiF and other fluorinated species in Li stripping/plating behavior (and battery performance in general), we believe that this correlation deserves further scrutiny.

In both our work and others,^{36,57} the SEI that forms in the presence of KPF₆ additive is consistently thinner than the SEI that forms in LP30 alone. Thinning of the SEI in the presence of KPF₆ is strikingly similar to observations from cells containing CsPF₆^{35,37} and RbPF₆³⁵ additives on Li metal as well as K acetate and Cs acetate additives on graphite anodes.⁵⁷ Taken together, these studies suggest that the alkali metal is critical for SEI composition and morphology, in particular because of the lack of discrimination of battery performance on additive anion (within a given alkali metal salt) or anode identity. In all cases, these alkali metal additives (K⁺, Rb⁺, and Cs⁺) exhibit lower reduction potentials (-2.88 V, -2.95 V, and -3.10 V vs SHE, respectively) than Li (-2.79 V vs SHE) in carbonate electrolytes,⁵⁸ suggesting that the additive cation does not plate on the surface of Li metal, consistent with our observations from DFT, EDS, and AAS. Instead, as we have shown for K⁺ additives, these alkali metals likely remain in solution while mediating electrolyte decomposition pathways through differential solvent adsorption at the electrode en route to forming a thinner SEI.

In addition to electrolyte adsorption, other parameters in a battery can lead to alternative electrolyte decomposition pathways that are not captured by DFT. For example, decomposition of the organic electrolyte (e.g. ring-opening of EC) may be the result of electrochemical cycling, surface defects, and different crystallographic facets on Li rather than adsorption. The ring-opening polymerization of EC to form a polycarbonate and PEO copolymer can be catalyzed by a range of Lewis acids, Lewis bases, and transition metals—some of which are alkali metal compounds^{59–61} or other salt decomposition products, such as PF₅.⁶² Copolymers that contain higher polycarbonate fractions are more amorphous, whereas PEO-based polymers are semi-crystalline.^{48,63} These differences in crystallinity may impact Li ion conductivity in the SEI on Li metal, making a polycarbonate-rich SEI more favorable for Li ion transport.⁶⁴ While high temperature solution phase polymerization reactions are an imperfect analogue to SEI formation on Li metal, multiple reports have shown that the polycarbonate:PEO ratio produced by ring-opening polymerization of EC depends on the identity of the alkali metal catalyst,^{59,60,65} with less acidic alkali metal carbonate catalysts (e.g. K₂CO₃, Rb₂CO₃, Cs₂CO₃) leading to higher polycarbonate:PEO ratios than *n*-BuLi. In the solid SEI on Li metal, K⁺ additives may play a similar role

in catalyzing the ring-opening polymerization of EC to favor polycarbonate moieties over PEO species (Figure S8). Likewise, DFT calculations show that K⁺ coordinates more strongly to the carbonyl oxygen in EC and DMC than does Li⁺. This preferred coordination between the carbonate solvent molecules and K⁺ can be rationalized by hard-soft acid-base (HSAB) theory.^{66,67} Both EC and DMC are characterized as soft bases due to their electrolyte stability windows,^{68,69} and K⁺ is a much softer acid than Li⁺.^{65,66} Therefore, the salt-solvent pair involving K⁺ is expected to be more stable than the pair involving Li⁺. This increased coordination with K⁺ may also suppress decarboxylation of polycarbonate species to form CO₂ and PEO, leading to the increased polycarbonate:PEO ratio that we observe in the K⁺-mediated SEI. These data suggest that KPF₆ additives may control electrolyte decomposition via adsorption at the electrolyte-electrode interface (as suggested by DFT) as well as reduce the amount of non-conductive species in the SEI (e.g. Li₂CO₃, PEO-rich polymers) to facilitate improved Li deposition.

CONCLUSIONS

We propose that tuning the cation composition of battery electrolyte formulations provides a new platform to control SEI composition and subsequent Li deposition morphology in Li metal batteries. Mechanistic insight from NMR spectroscopy, elemental analyses, and DFT calculations provided the framework to understand the connection between Li plating, SEI nature (i.e. stability, composition, thickness), and electrolyte decomposition. We show that cation identity and specifically, dual cation electrolytes where one ion is electrochemically inactive, can be leveraged to tune electrolyte adsorption at the electrolyte-electrode interface. Ion-solvent, solvent-electrode, and ion-solvent-electrode interactions are likely to depend strongly on cation identity and this approach has been relatively underexplored in the literature. In order to understand the relationship between cation engineering, SEI composition/thickness, and molecular-level ion-electrolyte-electrode interactions, a combination of high resolution characterization techniques that can quantitatively assess electrolyte decomposition and theory will be necessary going forward.

EXPERIMENTAL PROCEDURES

Materials and Methods

Lithium metal ribbon (0.75 mm thick), lithium hexafluorophosphate solution in 1:1 ethylene carbonate:dimethyl carbonate (1 M LiPF₆ in EC:DMC, LP30, battery grade), dimethyl carbonate (anhydrous, >99% and battery grade, ≥99.9%, acid <10 ppm, H₂O <10 ppm), ethylene carbonate (battery grade, ≥99%, acid <10 ppm, H₂O <10 ppm), ethylene carbonate-¹³C₃ (¹³C-labeled EC, 98 atom % ¹³C, 97% (CP)), dimethyl carbonate-¹³C₃ (¹³C-labeled DMC, 99 atom % ¹³C, 97% (CP)), lithium hexafluorophosphate (>99.99%, battery grade), potassium hexafluorophosphate (KPF₆, 99.50%, trace metals basis), TraceCERT AAS standards (Li, K, and Cs, 1000 mg/L, Supelco), and potassium bromide (KBr, 99%), were purchased from Sigma Aldrich. All items were used as received unless otherwise noted. Dimethyl sulfoxide-d₆ (DMSO-d₆, 99.9%) was purchased from Cambridge Isotope Laboratories. KBr was dried *in vacuo* for a week at 100 °C before bringing into an Ar-filled glovebox (<0.1 ppm O₂, <0.5 ppm H₂O). Both LiPF₆ and KPF₆ were dried *in vacuo* for 24 h at 100 °C before bringing into the glovebox. ¹³C-labeled EC and DMC were dried over molecular sieves for 48 h before using in battery cells.

Electrolyte formulations

Electrolytes of different compositions (LP30, LP30 + 0.1 M LiPF₆, LP30 + 0.1 M KPF₆, LP30 + 0.15 M KPF₆, LP30 + 0.25 M KPF₆) were prepared in an Ar-filled glovebox. ¹H NMR spectra were collected on LP30, LP30 + 0.1 M LiPF₆, and LP30 + 0.1 M KPF₆ electrolytes to check the purity and confirm that no water was present in both the battery-grade LP30 and the LiPF₆ and KPF₆ electrolyte salts, in addition to Karl Fischer titration measurements (Table S3). All electrolytes showed <10 ppm H₂O in Karl Fischer titration.

Electrochemical cycling

2032 Li/Li symmetric cells were assembled using Celgard 2325 separators or Whatman glass microfiber separators (GF/A) and electrolyte compositions listed above. Galvanostatic cycling experiments were performed at 1 mA cm⁻² for 2 h cycles or at 0.5 mA cm⁻² for 4 h cycles to pass the same amount of charge per experiment. Galvanostatic polarization experiments were performed at 1 mA cm⁻² for 2 h or at 0.5 mA cm⁻² for 4 h for the same reason. The electrochemistry for each characterization technique is described in detail in the corresponding subsection.

Solution NMR measurements

Electrolyte samples were prepared by assembling Li/Li symmetric coin cells with glass fiber separators. For each electrolyte composition, at least two independent battery cells were analyzed and compared. Electrolyte was then immediately extracted for pristine samples, whereas cycled samples were prepared by cycling the coin cell at 1 mA cm⁻² and 2 h charge/discharge cycles. Electrolyte was extracted by dipping Li electrodes and separator into 1.2 mL DMSO-d₆, and compressing the separator using clean tweezers to allow the electrolyte to dissolve in the DMSO-d₆. Electrolyte in DMSO-d₆ solution was then filtered using a 200 nm pore size polytetrafluoroethylene (PTFE) syringe filter to remove Li and glass fiber separator. Filtered samples were then sealed in 5 mm air-tight J Young tubes in the glovebox for data acquisition. Details on data acquisition can be found in the SI.

Solid-state NMR measurements

Individual samples were prepared by cycling 2032 Li/Li symmetric cells with Celgard 2325 separators at 1 mA cm⁻² for 2 h charge/discharge cycles. For each electrolyte composition, at least two independent battery cells were analyzed with . For ¹³C direct excitation experiments, 25% ¹³C₃-enriched EC/DMC were used in the electrolyte for 1 M LiPF₆ and 1 M LiPF₆ + 0.125 KPF₆ compositions. For all other experiments, non-enriched, battery grade electrolytes were used, unless otherwise noted. After cycling, microstructural Li was removed from the electrode surface using a razor blade, and dried *in vacuo* overnight in a glass vial. Microstructural Li was mixed thoroughly with KBr (5:1 or 10:1 w/w, depending on sample conductivity; see main text) using a mortar and pestle in the glovebox to limit electrical connectivity of conductive Li particles and reduce eddy currents⁴⁶ while spinning the sample in the NMR magnet before packing into a 1.6 mm o.d. ZrO₂ rotor. Higher samples dilutions were used to fill the volume of 3.2 mm o.d. ZrO₂ rotors for analysis with ¹⁹F SSNMR. Before loading into the SSNMR probehead, filled rotors were weighed to allow for quantitative comparison of the resulting SSNMR spectra. Details on data acquisition can be found in the SI.

Scanning electron microscopy and energy-dispersive X-ray spectroscopy

Scanning electron micrographs of the Li metal anode surface after galvanostatic polarization at 1 mA cm⁻² for 2 h were taken using a Zeiss Sigma VP Schottky Thermal Field emission SEM with a Gemini objective lens. Before imaging, all samples were washed by gently dipping in DMC to remove residual salts and prevent charging under the electron beam. Samples were dried *in vacuo* overnight to remove

residual electrolyte and solvent. Additional information on sample preparation and data analysis can be found in the SI. The samples were mounted on SEM stubs inside of the glovebox using carbon tape. Samples were transferred to the SEM sample chamber using an airtight Ar-filled jar, with exposure to atmosphere estimated to be <10 s for each sample. EDS was performed on the Zeiss SEM using a Bruker XFlash® 6 | 30 Detector on LP30 and LP30 + 0.1 M KPF₆ after cycling at 1 mA cm⁻² using 2 h charge/discharge cycles. Elemental maps for C, O, F, P, K, and a Si background were collected on both the Li electrode surface and electrode cross section.

DFT simulations

To model the electrolyte-surface interactions, self-consistent DFT calculations were carried out using the Perdew-Burke-Ernzerhof (PBE) generalized gradient approximation functional,⁷⁴ which is a GGA level functional, as implemented in the open-source package GPAW^{75,76}. The real-space grid spacing of 0.18 Å, and *k*-point grid (4, 4, 1) were used in the calculations, and the simulations were considered as converged for forces below 0.05 eV/Å. The atomic simulation environment (ASE)⁷⁷ was used to set up, manipulate, visualize and analyze the atomic structures. The bottom two layers on the *z*-axis of the Li slab were held fixed. Periodic boundary conditions were used for the *x* and *y* directions and a vacuum of 10 Å was used along the *z*-axis on both sides of the Li slab. In the initialized geometries, the electrolyte solvent and the alkali salt molecules were separated by at least 2 Å and constructed at least 2 Å above the Li surface. Bader charge analysis⁷⁸ (details in Supplementary Information, SI) was used to determine the amount of charge transferred from the Li surface to the alkali salt and solvent molecules in the final DFT optimized geometries. The dielectric constant of the electrolyte medium can modify the thermodynamics of the solvated species. However, it is widely accepted that simulations in vacuum without the explicit inclusion of solvent molecules provides a reasonable assumption because the solvent molecules are expected to play a minimal role in the vicinity of the solid-liquid interface⁷⁹.

ACKNOWLEDGMENTS

This work was funded by the Alfred P. Sloan Foundation through a Scialog: Advanced Energy Storage Collaborative Innovation Award, (2019-11419, LEM and VV). The authors thank Drs. Keith Fritzsching and Eric Keeler for assistance with SSNMR measurements. We thank Prof. Alan West for generously allowing us to use the atomic absorption spectrometer in his laboratory with the assistance of Mr. Jonathan Vardner. We thank Prof. Aaron Rossini for graciously providing the ¹H-detected ¹H-¹³C heteronuclear correlation pulse sequence used to collect the HETCOR data in this work.

AUTHOR CONTRIBUTIONS

Conceptualization, R.M., Y.Z., V.V., and L.E.M.; Methodology, R.M., Y.Z., V.V., and L.E.M.; Software, Y.Z. and V.V.; R.M. performed electrochemistry, NMR, SEM, AAS; Y.Z. performed DFT calculations; S.R.D. performed XPS; Writing—Original Draft, R.M. and L.E.M.; Writing—Review & Editing, R.M., Y.Z., S.R.D., V.V., and L.E.M.; Supervision, V.V. and L.E.M.; Funding Acquisition, V.V. and L.E.M.

DECLARATION OF INTERESTS

The authors declare no competing interests.

REFERENCES

1. Cheng, X.B., Zhang, R., Zhao, C.Z., and Zhang, Q. (2017). Toward Safe Lithium Metal Anode in Rechargeable Batteries: A Review. *Chem. Rev.* *117*, 10403–10473.
2. Liu, J., Bao, Z., Cui, Y., Dufek, E.J., Goodenough, J.B., Khalifah, P., Li, Q., Liaw, B.Y., Liu, P., Manthiram, A., et al. (2019). Pathways for practical high-energy long-cycling lithium metal batteries. *Nat. Energy* *4*, 180–186.
3. Zhang, S.S. (2013). Liquid electrolyte lithium/sulfur battery: Fundamental chemistry, problems, and solutions. *J. Power Sources* *231*, 153–162.
4. Girishkumar, G., McCloskey, B., Luntz, A.C., Swanson, S., and Wilcke, W. (2010). Lithium-air battery: Promise and challenges. *J. Phys. Chem. Lett.* *1*, 2193–2203.
5. Aurbach, D., McCloskey, B.D., Nazar, L.F., and Bruce, P.G. (2016). Advances in understanding mechanisms underpinning lithium-air batteries. *Nat. Energy* *1*, 1–11.
6. Kumar, N., Radin, M.D., Wood, B.C., Ogitsu, T., and Siegel, D.J. (2015). Surface-mediated solvent decomposition in Li-Air batteries: Impact of peroxide and superoxide surface terminations. *J. Phys. Chem. C* *119*, 9050–9060.
7. Janek, J., and Zeier, W.G. (2016). A solid future for battery development. *Nat. Energy* *1*, 1–4.
8. Yu, S., Park, H., and Siegel, D.J. (2019). Thermodynamic Assessment of Coating Materials for Solid-State Li, Na, and K Batteries. *ACS Appl. Mater. Interfaces* *11*, 36607–36615.
9. Bai, P., Li, J., Brushett, F.R., and Bazant, M.Z. (2016). Transition of lithium growth mechanisms in liquid electrolytes. *Energy Environ. Sci.* *9*, 3221–3229.
10. Wood, K.N., Kazyak, E., Chadwick, A.F., Chen, K.H., Zhang, J.G., Thornton, K., and Dasgupta, N.P. (2016). Dendrites and pits: Untangling the complex behavior of lithium metal anodes through operando video microscopy. *ACS Cent. Sci.* *11*, 790–801.
11. Fang, C., Wang, X., and Meng, Y.S. (2019). Key Issues Hindering a Practical Lithium-Metal Anode. *Trends Chem.* *1*, 152–158.
12. Choudhury, S., and Archer, L.A. (2016). Lithium Fluoride Additives for Stable Cycling of Lithium Batteries at High Current Densities. *Adv. Electron. Mater.* *2*, 1–7.
13. Chen, K.H., Sanchez, A.J., Kazyak, E., Davis, A.L., and Dasgupta, N.P. (2019). Synergistic Effect of 3D Current Collectors and ALD Surface Modification for High Coulombic Efficiency Lithium Metal Anodes. *Adv. Energy Mater.* *9*, 1802534.
14. Younesi, R., Veith, G.M., Johansson, P., Edström, K., and Vegge, T. (2015). Lithium salts for advanced lithium batteries: Li-metal, Li-O₂, and Li-S. *Energy Environ. Sci.* *8*, 1905–1922.
15. Chen, K.H., Wood, K.N., Kazyak, E., Lepage, W.S., Davis, A.L., Sanchez, A.J., and Dasgupta, N.P. (2017). Dead lithium: Mass transport effects on voltage, capacity, and failure of lithium metal anodes. *J. Mater. Chem. A* *5*, 11671–11681.
16. LePage, W.S., Chen, Y., Kazyak, E., Chen, K.-H., Sanchez, A.J., Poli, A., Arruda, E.M., Thouless, M.D., and Dasgupta, N.P. (2019). Lithium Mechanics: Roles of Strain Rate and Temperature and Implications for Lithium Metal Batteries. *J. Electrochem. Soc.* *166*, 89.
17. Tikekar, M.D., Choudhury, S., Tu, Z., and Archer, L.A. (2016). Design principles for electrolytes and interfaces for stable lithium-metal batteries. *Nat. Energy* *1*, 16114.

18. Cheng, X.B., Zhang, R., Zhao, C.Z., Wei, F., Zhang, J.G., and Zhang, Q. (2015). A review of solid electrolyte interphases on lithium metal anode. *Adv. Sci.* *3*, 1–20.
19. Bhowmik, A., Castelli, I.E., Garcia-Lastra, J.M., Jørgensen, P.B., Winther, O., and Vegge, T. (2019). A perspective on inverse design of battery interphases using multi-scale modelling, experiments and generative deep learning. *Energy Storage Mater.* *21*, 446–456.
20. Zhao, Q., Tu, Z., Wei, S., Zhang, K., Choudhury, S., Liu, X., and Archer, L.A. (2018). Building Organic/Inorganic Hybrid Interphases for Fast Interfacial Transport in Rechargeable Metal Batteries. *Angew. Chemie - Int. Ed.* *130*, 1004–1008.
21. Suo, L., Xue, W., Gobet, M., Greenbaum, S.G., Wang, C., Chen, Y., Yang, W., Li, Y., and Li, J. (2018). Fluorine-donating electrolytes enable highly reversible 5-V-class Li metal batteries. *Proc. Natl. Acad. Sci.* *115*, 1156–1161.
22. Qian, J., Henderson, W.A., Xu, W., Bhattacharya, P., Engelhard, M., Borodin, O., and Zhang, J. (2015). High rate and stable cycling of lithium metal anode. *Nat. Commun.* *6*, 6362.
23. Wang, J., Yamada, Y., Sodeyama, K., Chiang, C.H., Tateyama, Y., and Yamada, A. (2016). Superconcentrated electrolytes for a high-voltage lithium-ion battery. *Nat. Commun.* *7*, 12032.
24. Yamada, Y., Furukawa, K., Sodeyama, K., Kikuchi, K., Yaegashi, M., Tateyama, Y., and Yamada, A. (2014). Unusual stability of acetonitrile-based superconcentrated electrolytes for fast-charging lithium-ion batteries. *J. Am. Chem. Soc.* *136*, 5039–5046.
25. Yamada, Y., Usui, K., Chiang, C.H., Kikuchi, K., Furukawa, K., and Yamada, A. (2014). General observation of lithium intercalation into graphite in ethylene-carbonate-free superconcentrated electrolytes. *ACS Appl. Mater. Interfaces* *6*, 10892–10899.
26. Nie, M., Abraham, D.P., Seo, D.M., Chen, Y., Bose, A., and Lucht, B.L. (2013). Role of solution structure in solid electrolyte interphase formation on graphite with LiPF₆ in propylene carbonate. *J. Phys. Chem. C* *117*, 25381–25389.
27. Zhang, X.Q., Cheng, X.B., Chen, X., Yan, C., and Zhang, Q. (2017). Fluoroethylene Carbonate Additives to Render Uniform Li Deposits in Lithium Metal Batteries. *Adv. Funct. Mater.* *27*, 1605989.
28. Ota, H., Shima, K., Ue, M., and Yamaki, J. (2004). Effect of vinylene carbonate as additive to electrolyte for lithium metal anode. *Electrochim. Acta* *49*, 565–572.
29. Zhang, Y., and Krishnamurthy, D. (2020). Engineering Solid Electrolyte Interphase Composition by Assessing Decomposition Pathways of Fluorinated Organic Solvents in Lithium Metal Batteries. *J. Electrochem. Soc.* *167*, 070554.
30. Jin, Y., Kneusels, N.J.H., Marbella, L.E., Castillo-Martínez, E., Magusin, P.C.M.M., Weatherup, R.S., Jónsson, E., Liu, T., Paul, S., and Grey, C.P. (2018). Understanding Fluoroethylene Carbonate and Vinylene Carbonate Based Electrolytes for Si Anodes in Lithium Ion Batteries with NMR Spectroscopy. *J. Am. Chem. Soc.* *140*, 9854–9867.
31. Markevich, E., Salitra, G., and Aurbach, D. (2017). Fluoroethylene Carbonate as an Important Component for the Formation of an Effective Solid Electrolyte Interphase on Anodes and Cathodes for Advanced Li-Ion Batteries. *ACS Energy Lett.* *2*, 1337–1345.
32. Nakai, H., Kubota, T., Kita, A., and Kawashima, A. (2011). Investigation of the solid electrolyte interphase formed by fluoroethylene carbonate on Si electrodes. *J. Electrochem. Soc.* *158*, A798–A801.

33. Shkrob, I.A., Wishart, J.F., and Abraham, D.P. (2015). What Makes Fluoroethylene Carbonate Different? *J. Phys. Chem. C* *119*, 14954–14964.
34. Jung, R., Metzger, M., Haering, D., Solchenbach, S., Marino, C., Tsiovaras, N., Stinner, C., and Gasteiger, H.A. (2016). Consumption of fluoroethylene carbonate (FEC) on Si-C composite electrodes for Li-ion batteries. *J. Electrochem. Soc.* *163*, A1705–A1716.
35. Ding, F., Xu, W., Graff, G.L., Zhang, J., Sushko, M.L., Chen, X., Shao, Y., Engelhard, M.H., Nie, Z., Xiao, J., et al. (2013). Dendrite-free lithium deposition via self-healing electrostatic shield mechanism. *J. Am. Chem. Soc.* *115*, 4450–4456.
36. Wood, S.M., Pham, C.H., Rodriguez, R., Nathan, S.S., Dolocan, A.D., Celio, H., De Souza, J.P., Klavetter, K.C., Heller, A., and Mullins, C.B. (2016). K⁺ Reduces Lithium Dendrite Growth by Forming a Thin, Less-Resistive Solid Electrolyte Interphase. *ACS Energy Lett.* *1*, 414–419.
37. Wang, X., Zhang, M., Alvarado, J., Wang, S., Sina, M., Lu, B., Bouwer, J., Xu, W., Xiao, J., Zhang, J.G., et al. (2017). New Insights on the Structure of Electrochemically Deposited Lithium Metal and Its Solid Electrolyte Interphases via Cryogenic TEM. *Nano Lett.* *17*, 7606–7612.
38. Zhang, Y., Qian, J., Xu, W., Russell, S.M., Chen, X., Nasybulin, E., Bhattacharya, P., Engelhard, M.H., Mei, D., Cao, R., et al. (2014). Dendrite-free lithium deposition with self-aligned nanorod structure. *Nano Lett.* *14*, 6889–6896.
39. Andrew, E.R., Corolan, J.L., and Randall, P.J. (1971). More precise knight shift measurements: Application to copper. *Phys. Lett. A* *35*, 435–436.
40. Zhu, Y., Pande, V., Li, L., Pan, S., Wen, B., Wang, D., Viswanathan, V., and Chiang, Y.-M. (2019). Design Principles for Self-forming Interfaces Enabling Stable Lithium Metal Anodes. arXiv:1903.09593 [physics].
41. Fang, C., Li, J., Zhang, M., Zhang, Y., Yang, F., Lee, J.Z., Lee, M.-H., Alvarado, J., Schroeder, M.A., Yang, Y., et al. (2019). Quantifying inactive lithium in lithium metal batteries. *Nature* *572*, 511–515.
42. Bai, P., Li, J., Brushett, F.R., and Bazant, M.Z. (2016). Transition of lithium growth mechanisms in liquid electrolytes. *Energy Environ. Sci.* *9*, 3221–3229.
43. Xu, K., Zhuang, G. V., Allen, J.L., Lee, U., Zhang, S.S., Ross, P.N., and Jow, T.R. (2006). Syntheses and characterization of lithium alkyl mono- and bicarbonates as components of surface films in Li-ion batteries. *J. Phys. Chem. B* *110*, 7708–7719.
44. Campion, C.L., Li, W., and Lucht, B.L. (2005). Thermal decomposition of LiPF₆-based electrolytes for lithium-ion batteries. *J. Electrochem. Soc.* *152*, 2327–2334.
45. Jin, Y., Kneusels, N.J.H., Magusin, P.C.M.M., Kim, G., Castillo-Martínez, E., Marbella, L.E., Kerber, R.N., Howe, D.J., Paul, S., Liu, T., et al. (2017). Identifying the Structural Basis for the Increased Stability of the Solid Electrolyte Interphase Formed on Silicon with the Additive Fluoroethylene Carbonate. *J. Am. Chem. Soc.* *139*, 14992–15004.
46. Aguiar, P.M., Jacquinot, J.F., and Sakellariou, D. (2009). Experimental and numerical examination of eddy (Foucault) currents in rotating micro-coils: Generation of heat and its impact on sample temperature. *J. Magn. Reson.* *200*, 6–14.
47. Leskes, M., Kim, G., Liu, T., Michan, A.L., Aussénac, F., Dorffer, P., Paul, S., and Grey, C.P. (2017). Surface-Sensitive NMR Detection of the Solid Electrolyte Interphase Layer on Reduced Graphene Oxide. *J. Phys. Chem. Lett.* *8*, 1078–1085.

48. Park, Y., Shin, S.H., Hwang, H., Lee, S.M., Kim, S.P., Choi, H.C., and Jung, Y.M. (2014). Investigation of solid electrolyte interface (SEI) film on LiCoO₂ cathode in fluoroethylene carbonate (FEC)-containing electrolyte by 2D correlation X-ray photoelectron spectroscopy (XPS). *J. Mol. Struct.* *1069*, 157–163.
49. Michan, A.L., Divitini, G., Pell, A.J., Leskes, M., Ducati, C., and Grey, C.P. (2016). Solid Electrolyte Interphase Growth and Capacity Loss in Silicon Electrodes. *J. Am. Chem. Soc.* *138*, 7918–7931.
50. Shi, S., Qi, Y., Li, H., and Hector, L.G. (2013). Defect Thermodynamics and Diffusion Mechanisms in Li₂CO₃ and Implications for the Solid Electrolyte Interphase in Li-Ion Batteries. *J. Phys. Chem. C* *117*, 8579–8593.
51. Nagy, K.S., Kazemiabnavi, S., Thornton, K., and Siegel, D.J. (2019). Thermodynamic Overpotentials and Nucleation Rates for Electrodeposition on Metal Anodes. *ACS Appl. Mater. Interfaces* *11*, 7954–7964.
52. Bader, R.F.W., and MacDougall, P.J. (1985). Toward a Theory of Chemical Reactivity Based on the Charge Density. *J. Am. Chem. Soc.* *107*, 6788–6795.
53. Bale, C.W. (1989). The K-Li (Potassium-Lithium) System. *Bull. Alloy Phase Diagrams* *10*, 262–264.
54. Gagné, O.C., and Hawthorne, F.C. (2016). Bond-length distributions for ions bonded to oxygen: alkali and alkaline-earth metals. *Acta Crystallogr. B. Struct. Sci. Cryst. Eng. Mater.* *72*, 602–625.
55. Wenger, M., and Armbruster, T. (1991). Crystal chemistry of lithium; oxygen coordination and bonding. *Eur. J. Mineral.* *3*, 387–399.
56. Bondi, A. (1964). Van der waals volumes and radii. *J. Phys. Chem.* *68*, 441–451.
57. Chandrasiri, K.W.D.K., Nguyen, C.C., Zhang, Y., Parimalam, B.S., and Lucht, B.L. (2017). Systematic Investigation of Alkali Metal Ions as Additives for Graphite Anode in Propylene Carbonate Based Electrolytes. *Electrochim. Acta*.
58. Marcus, Y. (1985). International union of pure and applied chemistry:Analytical chemistry division commission on electro analytical chemistry thermodynamic functions of transfer of single ions from water to nonaqueous and mixed solvents part 3: Standard potentials of select. *Pure Appl. Chem.* *57*, 1129–1132.
59. Vogdanis, L., and Heitz, W. (1986). Carbon dioxide as a monomer, 3. The polymerization of ethylene carbonate. *Die Makromol. Chemie, Rapid Commun.* *7*, 543–547.
60. Soga, K., Tazuke, Y., Hosada, S., and Ikeda, S. (1977). Polymerization of Propylene Carbonate. *J Polym Sci Polym Chem Ed* *15*, 219–229.
61. Lee, J.C., and Litt, M.H. (2000). Ring-opening polymerization of ethylene carbonate and depolymerization of poly(ethylene oxide-co-ethylene carbonate). *Macromolecules* *33*, 1618–1627.
62. Sloop, S.E., Kerr, J.B., and Kinoshita, K. (2003). The role of Li-ion battery electrolyte reactivity in performance decline and self-discharge. *J. Power Sources* *119–121*, 330–337.
63. Kwon, S.J., Kim, D.G., Shim, J., Lee, J.H., Baik, J.H., and Lee, J.C. (2014). Preparation of organic/inorganic hybrid semi-interpenetrating network polymer electrolytes based on poly(ethylene oxide-co-ethylene carbonate) for all-solid-state lithium batteries at elevated temperatures. *Polym. J.* *55*, 2799–2808.

64. Cheng, S., Smith, D.M., and Li, C.Y. (2014). How Does Nanoscale Crystalline Structure Affect Ion Transport in Solid Polymer Electrolytes?. *Macromolecules* *47*, 3978–3986.
65. Pawłowski, P., and Rokicki, G. (2004). Synthesis of oligocarbonate diols from ethylene carbonate and aliphatic diols catalyzed by alkali metal salts. *Polym. J.* *45*, 3125–3137.
66. Pearson, R.G. (1988). Absolute Electronegativity and Hardness: Application to Inorganic Chemistry. *Inorg. Chem.* *27*, 734–740.
67. Parr, R.G., and Pearson, R.G. (1983). Absolute Hardness: Companion Parameter to Absolute Electronegativity. *J. Am. Chem. Soc.* *105*, 7512–7516.
68. Su, C.C., He, M., Amine, R., Chen, Z., and Amine, K. (2018). The Relationship between the Relative Solvating Power of Electrolytes and Shuttling Effect of Lithium Polysulfides in Lithium–Sulfur Batteries. *Angew. Chemie - Int. Ed.*
69. Haruna, H., Takahashi, S., and Tanaka, Y. (2017). Accurate Consumption Analysis of Vinylene Carbonate as an Electrolyte Additive in an 18650 Lithium-Ion Battery at the First Charge–Discharge Cycle. *J. Electrochem. Soc.* *164*, A6278–A6280.
70. Venkatesh, A., Ryan, M.J., Biswas, A., Boteju, K.C., Sadow, A.D., and Rossini, A.J. (2018). Enhancing the Sensitivity of Solid-State NMR Experiments with Very Low Gyromagnetic Ratio Nuclei with Fast Magic Angle Spinning and Proton Detection. *J. Phys. Chem. A* *122*, 5635–5643.
71. Eshetu, G.G., Diemant, T., Grugeon, S., Behm, R.J., Laruelle, S., Armand, M., and Passerini, S. (2016). In-Depth Interfacial Chemistry and Reactivity Focused Investigation of Lithium-Imide- and Lithium-Imidazole-Based Electrolytes. *ACS Appl. Mater. Interfaces* *8*, 16087–16100.
72. Karpiuk, U.V., Mohammad, K., Azzam, A., Helmi, Z., and Abudayeh, M. (2016). Qualitative and Quantitative Content Determination of Macro - Minor Elements in Bryonia Alba L . Roots using Flame Atomic Absorption Spectroscopy Technique. *Tabriz Univ. Med. Sci.* *6*, 285–291.
73. Schneider, C.A., Rasband, W.S., and Eliceiri, K.W. (2012). NIH Image to ImageJ: 25 years of image analysis. *Nat. Methods* *9*, 671–675.
74. Perdew, J.P., Burke, K., and Ernzerhof, M. (1996). Generalized Gradient Approximation Made Simple. *Phys. Rev. Lett.* *77*, 3865–3868.
75. Mortensen, J.J., Hansen, L.B., and Jacobsen, K.W. (2005). Real-space grid implementation of the projector augmented wave method. *Phys. Rev. B* *71*, 35109.
76. Enkovaara, J., Rostgaard, C., Mortensen, J.J., Chen, J., Dułak, M., Ferrighi, L., Gavnholt, J., Glinsvad, C., Haikola, V., Hansen, H.A., et al. (2010). Electronic structure calculations with GPAW: A real-space implementation of the projector augmented-wave method. *J. Phys. Condens. Matter* *22*, 253202.
77. Larsen, A.H. (2009). Localized Atomic Orbital Basis Sets in the Projector Augmented Wave Method. *Phys. Rev. B - Condens. Matter Mater. Phys.* *80*, 195112.
78. Tang, W., Sanville, E., and Henkelman, G. (2009). A grid-based Bader analysis algorithm without lattice bias. *J. Phys. Condens. Matter* *21*, 84204.
79. Khetan, A., Pitsch, H., and Viswanathan, V. (2014). Identifying descriptors for solvent stability in nonaqueous Li–O₂ batteries. *J. Phys. Chem. Lett.* *5*, 1318–1323.

Supplementary Information: Leveraging Cation Identity to Engineer Solid Electrolyte Interphases for Rechargeable Lithium Metal Anodes

Richard May,⁴ Yumin Zhang,⁵ Steven R. Denny,⁴ Venkatasubramanian Viswanathan,^{5,6,*} Lauren E. Marbella^{4,*}

Table of Contents

Supplemental Data Items

| | |
|--|-----------|
| Electrochemical Measurements | 19 |
| Solution NMR | 21 |
| Solid-state NMR | 27 |
| X-ray photoelectron spectroscopy..... | 32 |
| Energy-dispersive X-ray spectroscopy..... | 33 |
| Atomic absorption spectroscopy..... | 35 |
| KF Titration..... | 36 |
| DFT..... | 36 |
| Scanning electron microscopy..... | 37 |

Supplemental Experimental Procedures

| | |
|---|-----------|
| Analysis of scanning electron micrographs..... | 38 |
| Coulombic efficiency measurements | 38 |
| Solution NMR..... | 38 |
| Solid-state NMR..... | 39 |
| X-ray photoelectron spectroscopy..... | 39 |
| Atomic absorption spectroscopy..... | 40 |
| Calculation of Bader Charge Transfers..... | 40 |

| | |
|-------------------------------------|-----------|
| Supplemental References..... | 40 |
|-------------------------------------|-----------|

⁴ Department of Chemical Engineering, Columbia University, New York, New York 10027, United States

⁵ Department of Materials Science and Engineering, Carnegie Mellon University, Pittsburgh, Pennsylvania 15213, United States

⁶ Department of Mechanical Engineering, Carnegie Mellon University, Pittsburgh, Pennsylvania 15213, United States

*Correspondence: venkvis@cmu.edu, lem2221@columbia.edu

Supplemental Data Items

Electrochemical Measurements

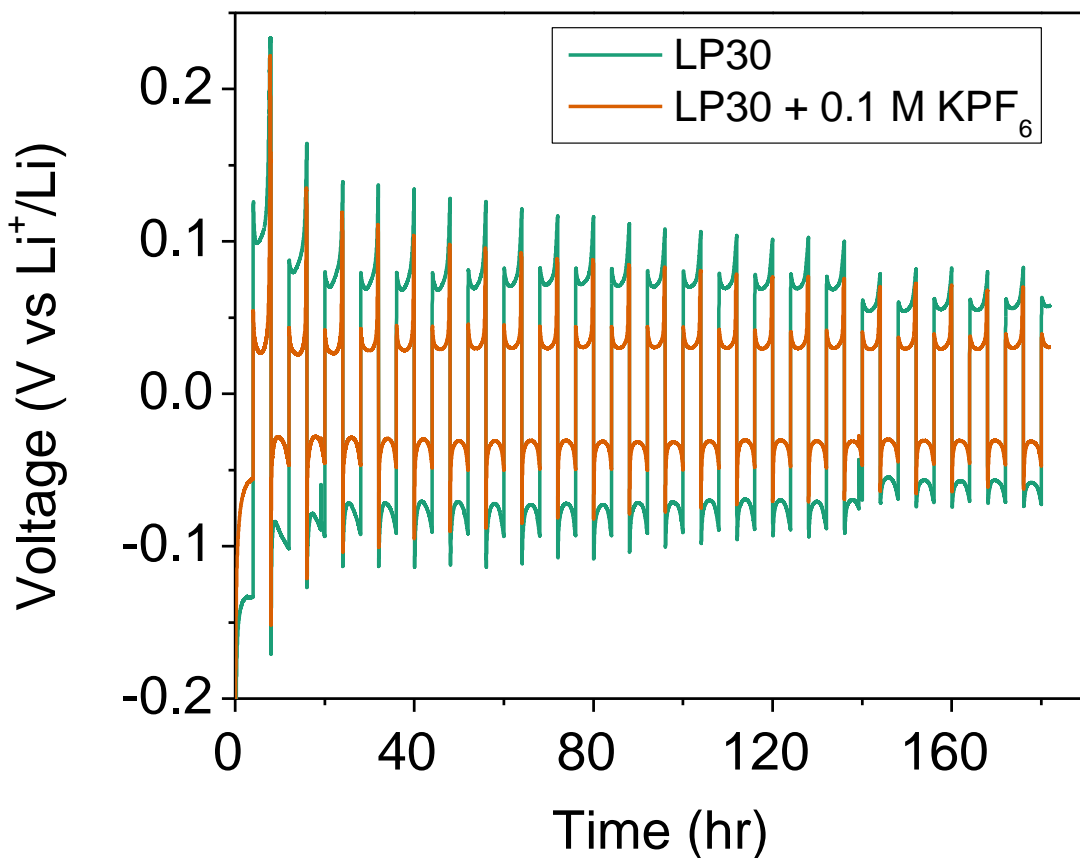


Figure S1. Voltage profile for Li/Li symmetric coin cells galvanostatically cycled at 0.5 mA cm^{-2} for 4 h cycles (LP30 = green, LP30 + 0.1 M KPF₆ = orange). While a lower overpotential for KPF₆ containing electrolytes is shown here, overpotentials between LP30 and LP30 + KPF₆ were relatively similar between individual trials and showed comparable voltage profiles.

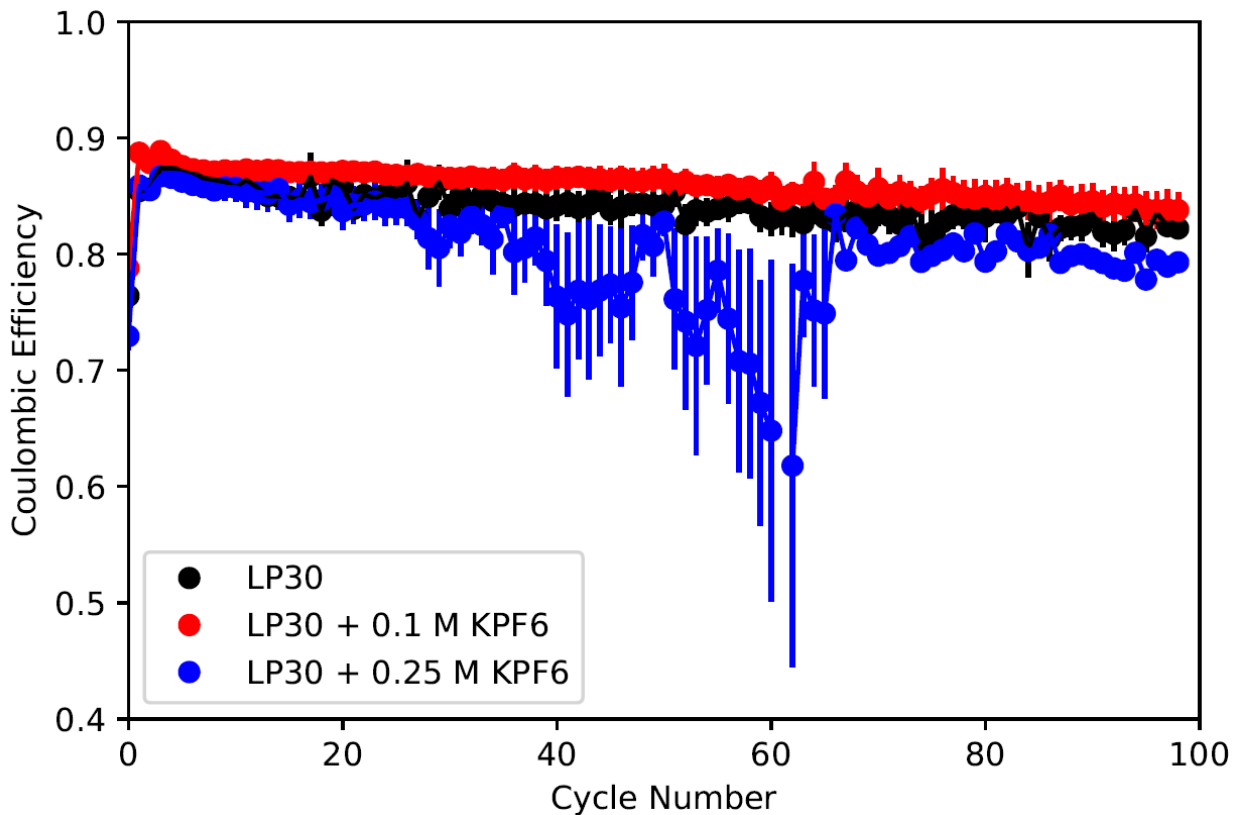


Figure S2. Coulombic efficiency measurements for Li/Cu coin cells cycled in LP30 (black), LP30 + 0.1 M KPF₆ (red), and LP30 + 0.25 M KPF₆ (blue). Error bars represent standard error for N = 3.

Solution NMR

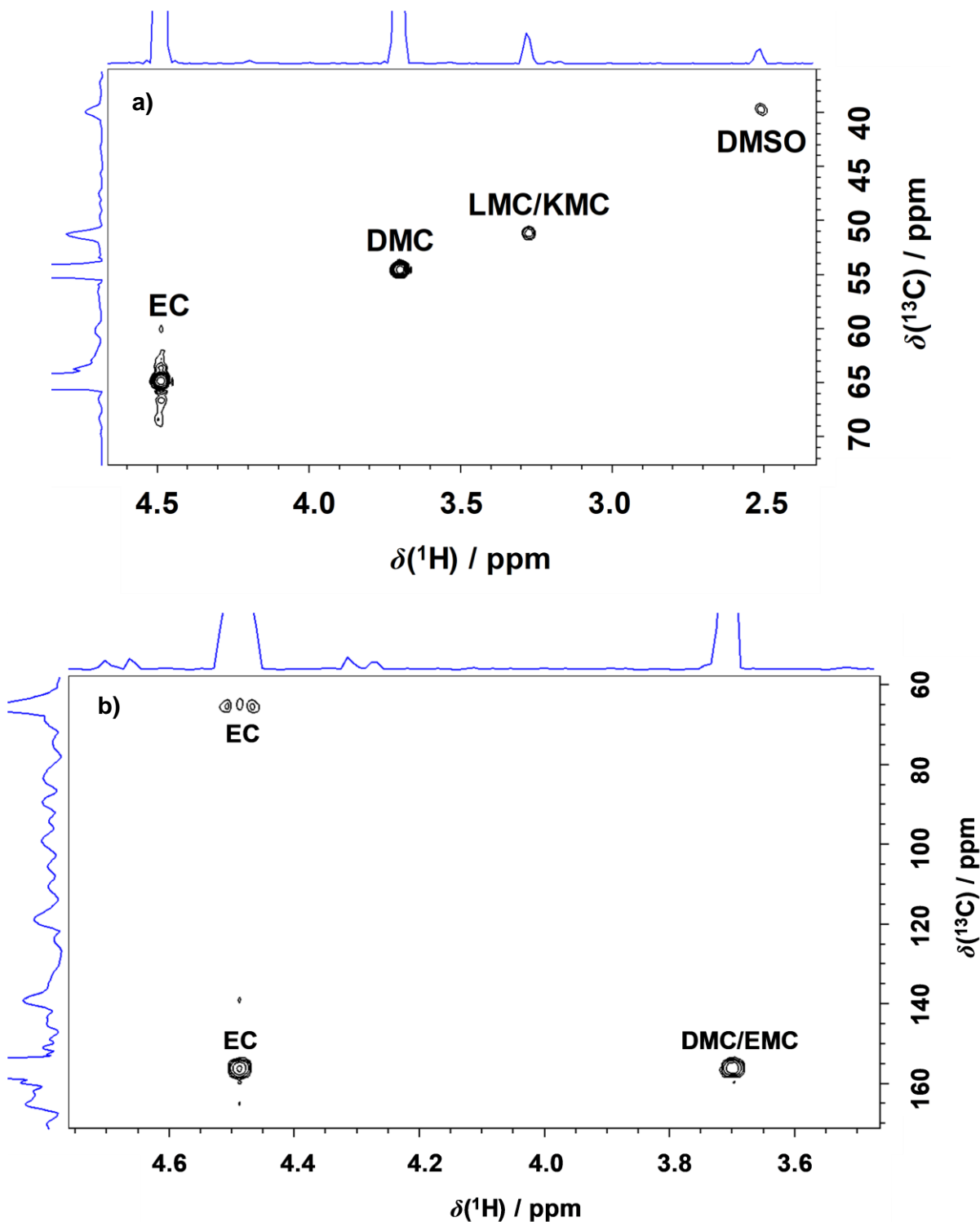


Figure S3. ^1H - ^{13}C correlation NMR spectra of the cycled LP30 electrolyte extracted from Li symmetric cells after 94 cycles. a) HSQC, b) HMBC.

The singlet ^1H resonance at 4.49 ppm assigned to EC is directly bound to a carbon with a chemical shift of 64.9 ppm (Figure S3a) and correlated with a carbonyl carbon at \sim 156 ppm (Figure S3b). The singlet ^1H resonance at 3.70 ppm assigned to DMC/EMC is directly bound to a carbon with a chemical shift of 54.5 ppm (Figure S3a) and correlated with a carbonyl carbon at \sim 156 ppm (Figure S3b). The singlet ^1H resonance at 3.27 ppm assigned to LMC is directly bound to a carbon at 51 ppm. Ethyl protons corresponding to EMC are likely present in small quantities undetectable using 2D correlation methods. Solvent peaks are cut off to highlight smaller peaks assigned to decomposition products. Related to Figure 2.

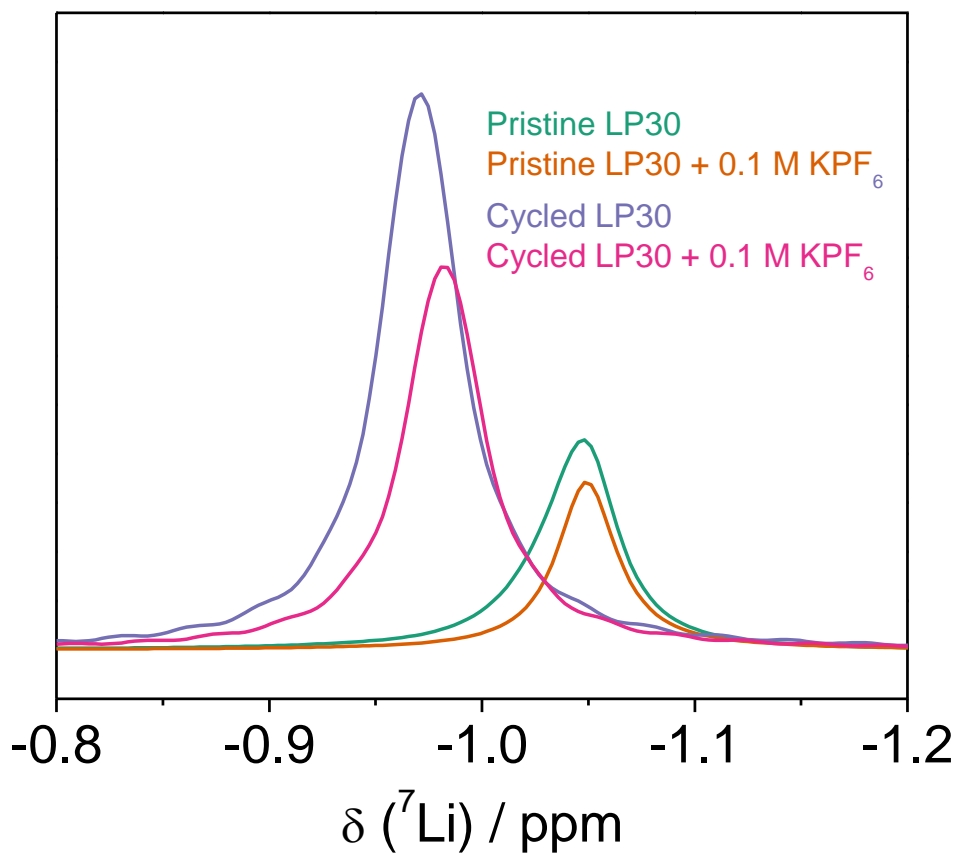


Figure S4. ^7Li solution NMR for pristine electrolytes and electrolyte extracted after 94 cycles (LP30 and LP30 + 0.1 M KPF_6). Related to Figure 2.

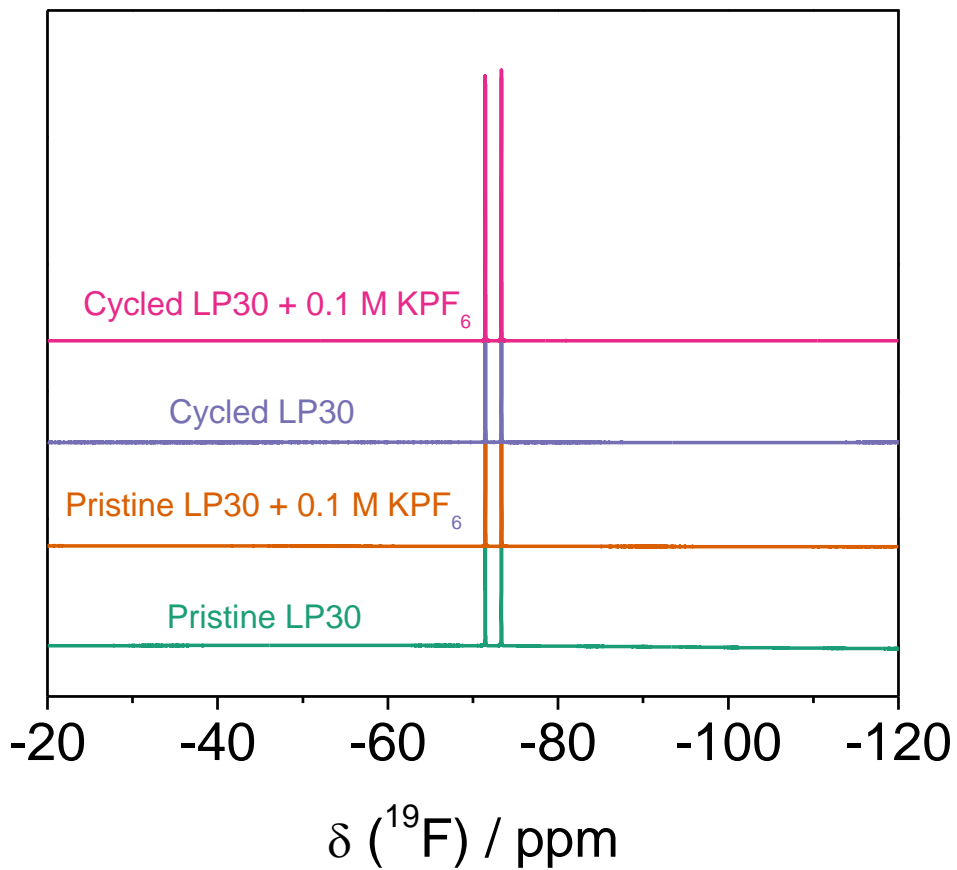


Figure S5. ^{19}F solution NMR for pristine electrolytes and electrolyte extracted after 94 cycles (LP30 and LP30 + 0.1 M KPF_6). Doublet at -72.4 ppm corresponds to PF_6^- . Related to Figure 2.

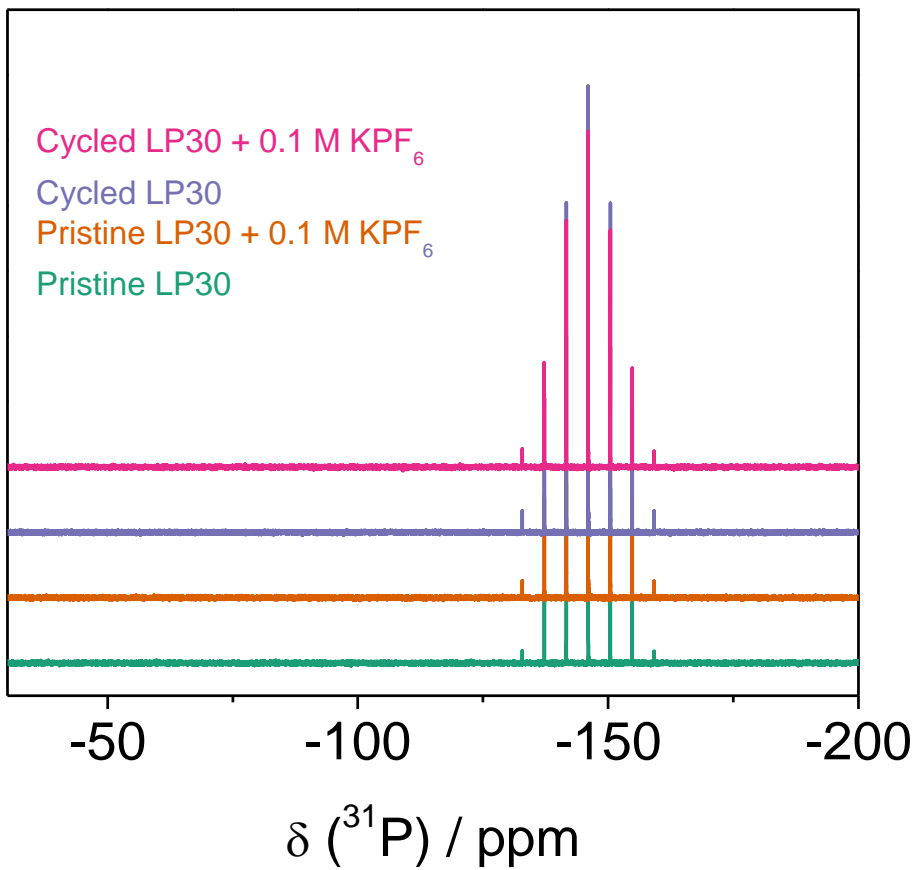


Figure S6. ^{31}P solution NMR for pristine electrolytes and electrolyte extracted after 94 cycles (LP30 and LP30 + 0.1 M KPF₆). Septet at -146 ppm corresponds to PF₆⁻. Related to Figure 2.

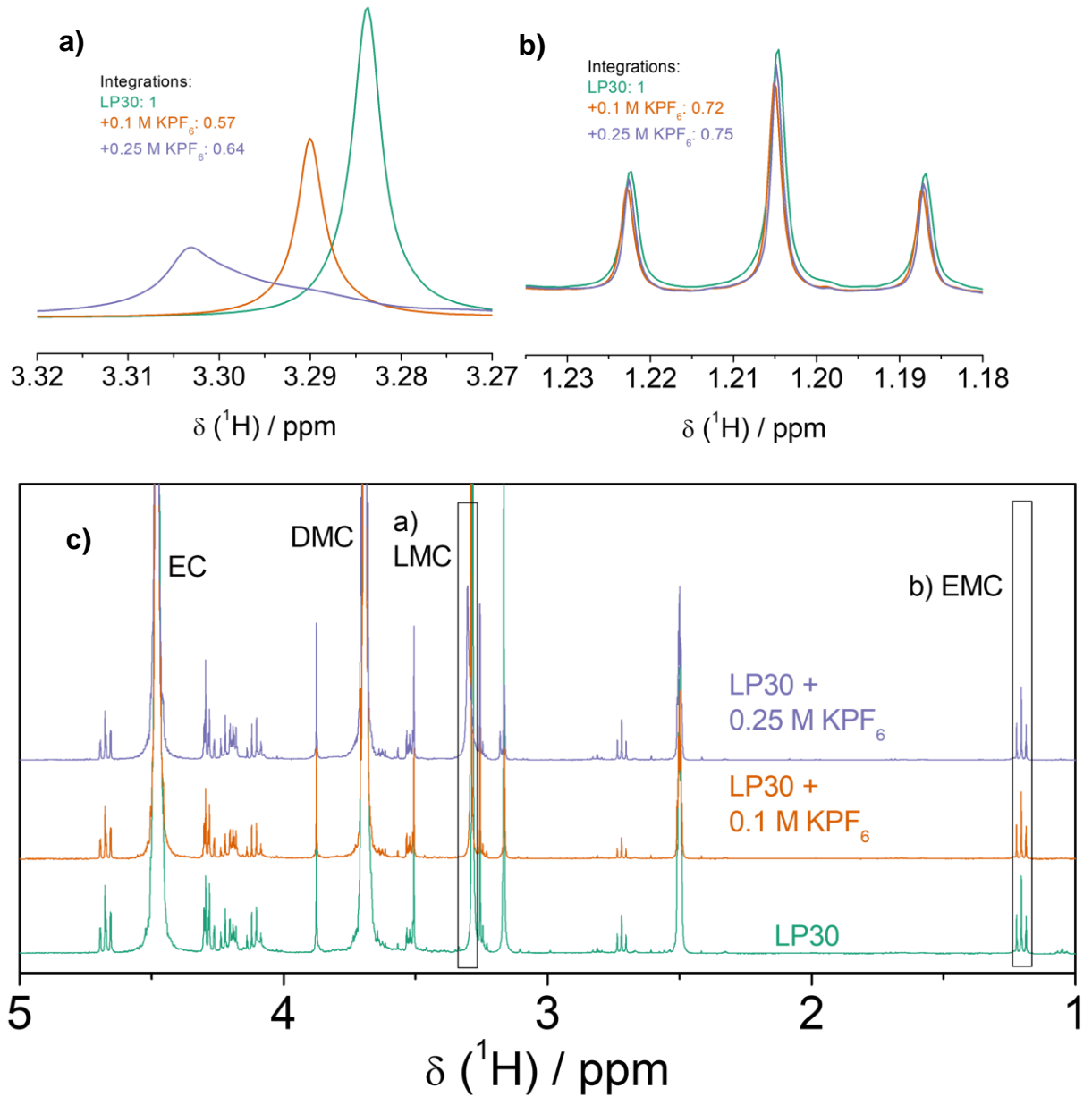


Figure S7. ¹H solution NMR for electrolyte extracted from Li/Li symmetric cells after 50 cycles in LP30 (green), LP30 + 0.1 M KPF₆ (orange), and LP30 + 0.25 M KPF₆ (purple). a) Singlets at ~3.3 ppm which correspond to KMC/LMC. b) Triplet at 1.2 ppm corresponding to EMC. c) Full spectra for LP30, LP30 + 0.1 M KPF₆, and LP30 + 0.25 M KPF₆. Resonances at 1.20 (t , $J_{HH} = 7.1$ Hz), 3.69 ppm (s), 4.11 ppm (q, $J_{HH} = 7.1$ Hz) correspond to EMC and the singlet at ~3.27 ppm corresponds to LMC/KMC. Major peaks at 4.5 ppm and 3.7 ppm correspond to EC and DMC/EMC respectively. Based on peak integrations for major decomposition products LMC and EMC, LP30 + 0.1 M KPF₆ yields the least decomposition as compared to LP30 and LP30 + 0.25 M KPF₆.

Table S1. Peak assignments for ^1H and ^{13}C solution NMR of the soluble SEI (Figure 2, Figure S8).

| Functional group | Assignment | ^1H shift | J_{HH} | ^{13}C shift |
|---------------------------|------------|--------------------|------------------------------------|-----------------------|
| ROCO₂Li | LMC | N/A | N/A | 156.3 |
| ROCO₂R' | EC | N/A | N/A | 155.8 |
| ROCO₂R' | DMC/EMC | N/A | N/A | 155.6 |
| RCH₂O- | EC | 4.48 | s | 65.0 |
| RCH₂O- | EMC | 4.11 | q, $\text{J}_{\text{HH}} = 7.1$ Hz | 63.6 |
| CH₂O- | DMC | 3.69 | s | 54.7 |
| CH₂O- | LMC | 3.27 | s | 51.2 |
| CH₃R- | EMC | 1.20 | t, $\text{J}_{\text{HH}} = 7.1$ Hz | 14.1 |

Solid-state NMR

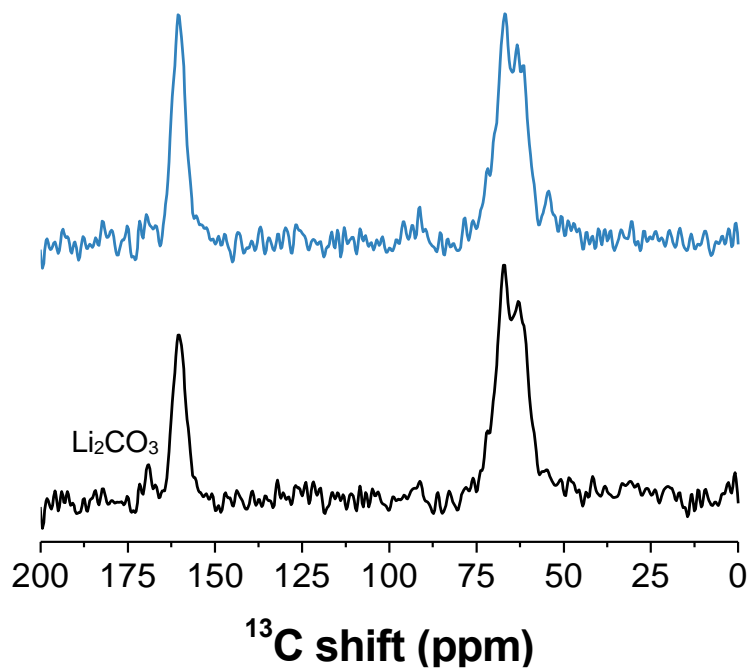


Figure S8. ^{13}C direct polarization SSNMR of solid electrolyte decomposition products for LP30 (black) and LP30 + 0.1 M KPF₆ (blue) electrolytes using 25% v/v ^{13}C -enriched EC and DMC collected at MAS = 18 kHz at room temperature. LP30 + 0.1 M KPF₆ shows higher amounts of polycarbonate (~160 ppm) and less PEO species (~70 ppm) compared to LP30. The presence of Li₂CO₃ (~170 ppm) is evident in LP30 electrolytes.

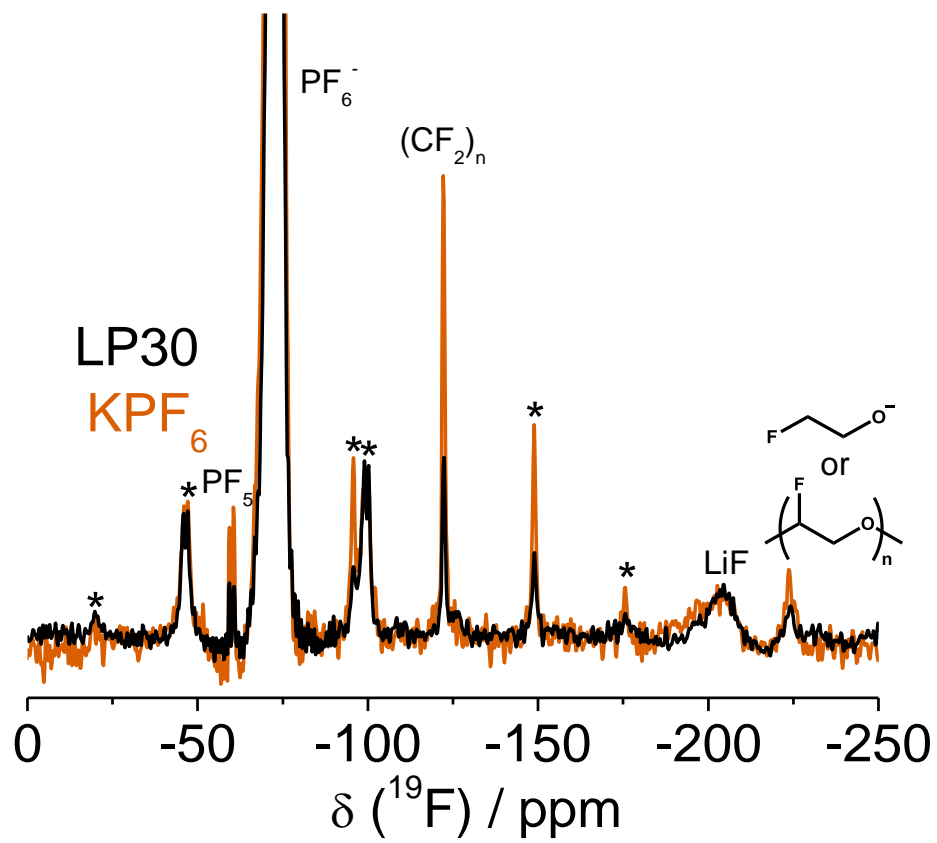


Figure S9. MAS ^{19}F NMR (MAS = 15 kHz) of electrolyte decomposition products for LP30 (black) and LP30 + 0.1 M KPF₆ (orange) after 94 cycles. Major decomposition products include LiF (reference, singlet, -204 ppm), PF₅ (doublet, -60 ppm), and CH₂FCH₂OR (singlet, -224 ppm). Asterisks denote spinning sidebands. Related to Figure 3.

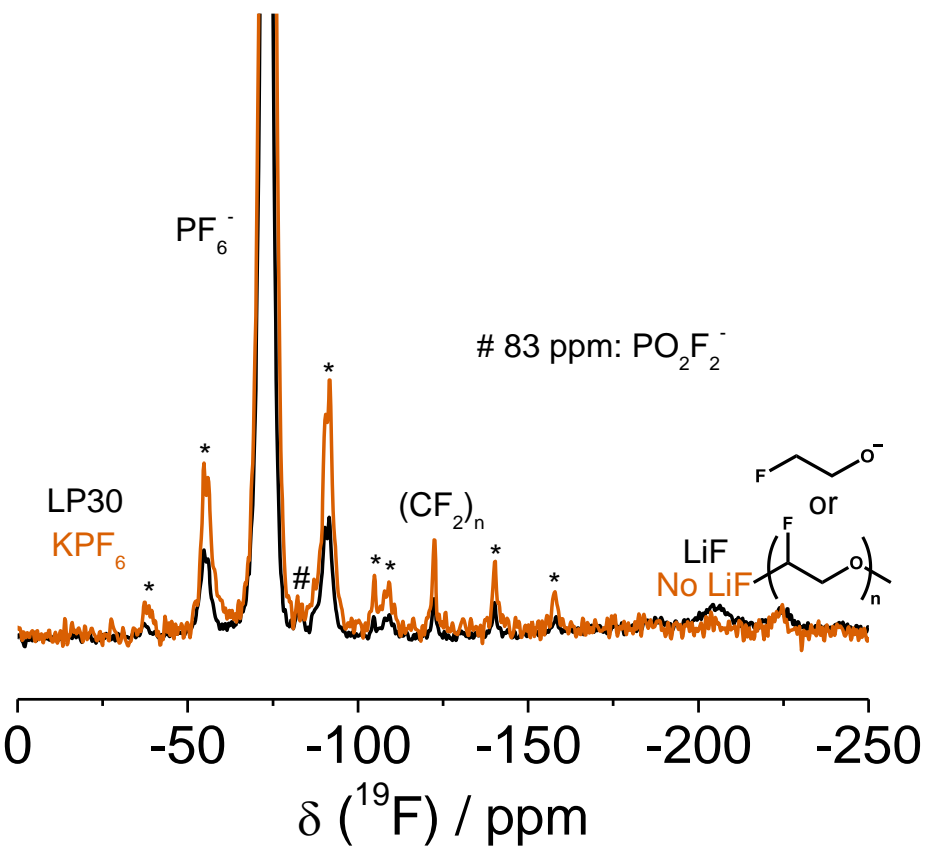


Figure S10. ^{19}F NMR (MAS = 10 kHz) of electrolyte decomposition products for LP30 (black) and LP30 + 0.1 M KPF_6 (orange) using 25% ^{13}C -labeled EC and DMC electrolyte solvents after 94 cycles. Major decomposition products include LiF (reference, singlet, -204 ppm), PO_2F_2^- (singlet, -83 ppm), $(\text{CF}_2)_n$ (-122 ppm) and $\text{CH}_2\text{FCH}_2\text{OR}$ (singlet, -224 ppm). Asterisks denote spinning sidebands.

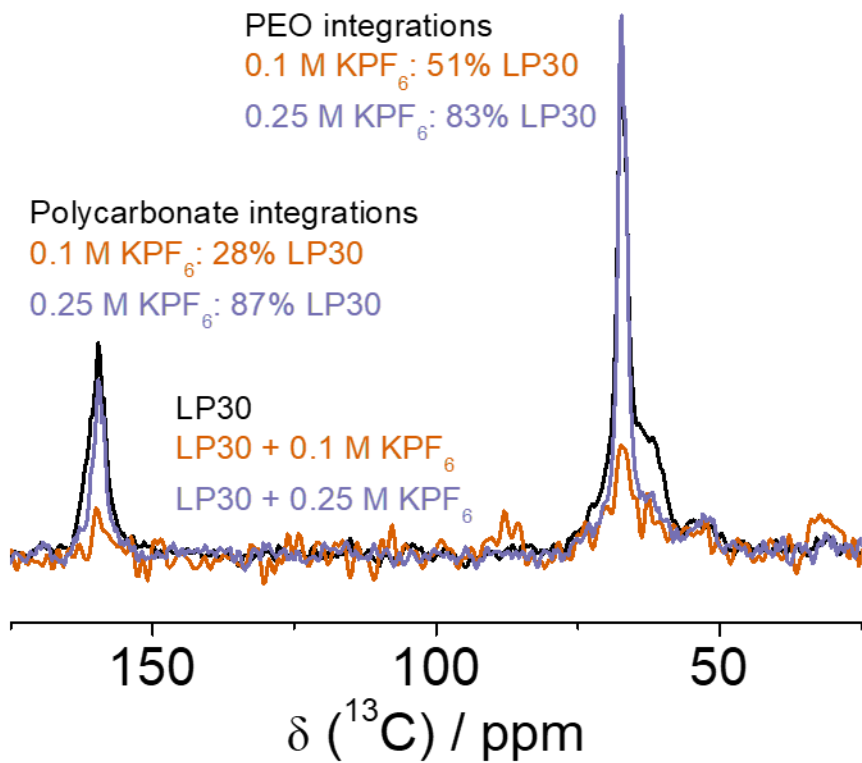
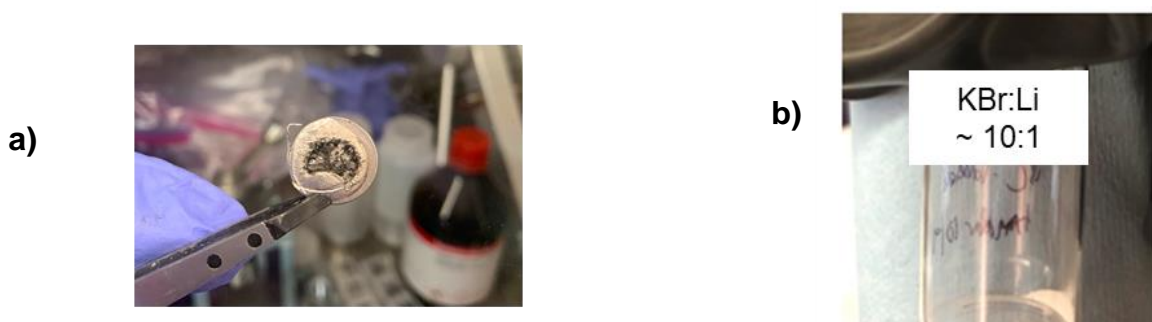


Figure S11. Solid-state CPMAS ^{13}C NMR of electrolyte decomposition products for LP30 (black), LP30 + 0.1 M KPF_6 (orange), and LP30 + 0.25 M KPF_6 (purple) after 50 cycles. Major decomposition products include polycarbonate and PEO-type species, and less decomposition is observed after KPF_6 addition. Li acetate and Li succinate are either not formed in the SEI or below the detection limit of the experiment.



Mix with non-metallic matrix to allow MAS

Figure S12. Depiction of sample preparation for SSNMR of the SEI on Li metal.

After extensive cycling, the surface of the Li metal electrode was covered in a dark, soft microstructural layer where the bulk of the SEI resides (Schematic 1a). This microstructural layer was then isolated as best as possible from the bulk Li (which looked more metallic and reflective than the microstructural layer) and allowed to dry *in vacuo* overnight in a vial to remove electrolyte solvent.

After drying, these microstructures were still darker and softer than the bulk Li metal. If pieces of hard, reflective Li metal pieces were interspersed with the microstructural Li, they were selectively removed to mitigate the formation of eddy currents during the SSNMR experiment. After mixing the microstructural Li with KBr, the resulting powder was grey and uniform in both color and consistency (Schematic 1b). This powder was then directly packed into a rotor. All steps were performed in Ar atmosphere with KBr that had been thoroughly dried *in vacuo* at 100 °C.

This procedure was used to prepare samples for SSNMR as shown in Figure 3.

X-ray photoelectron spectroscopy

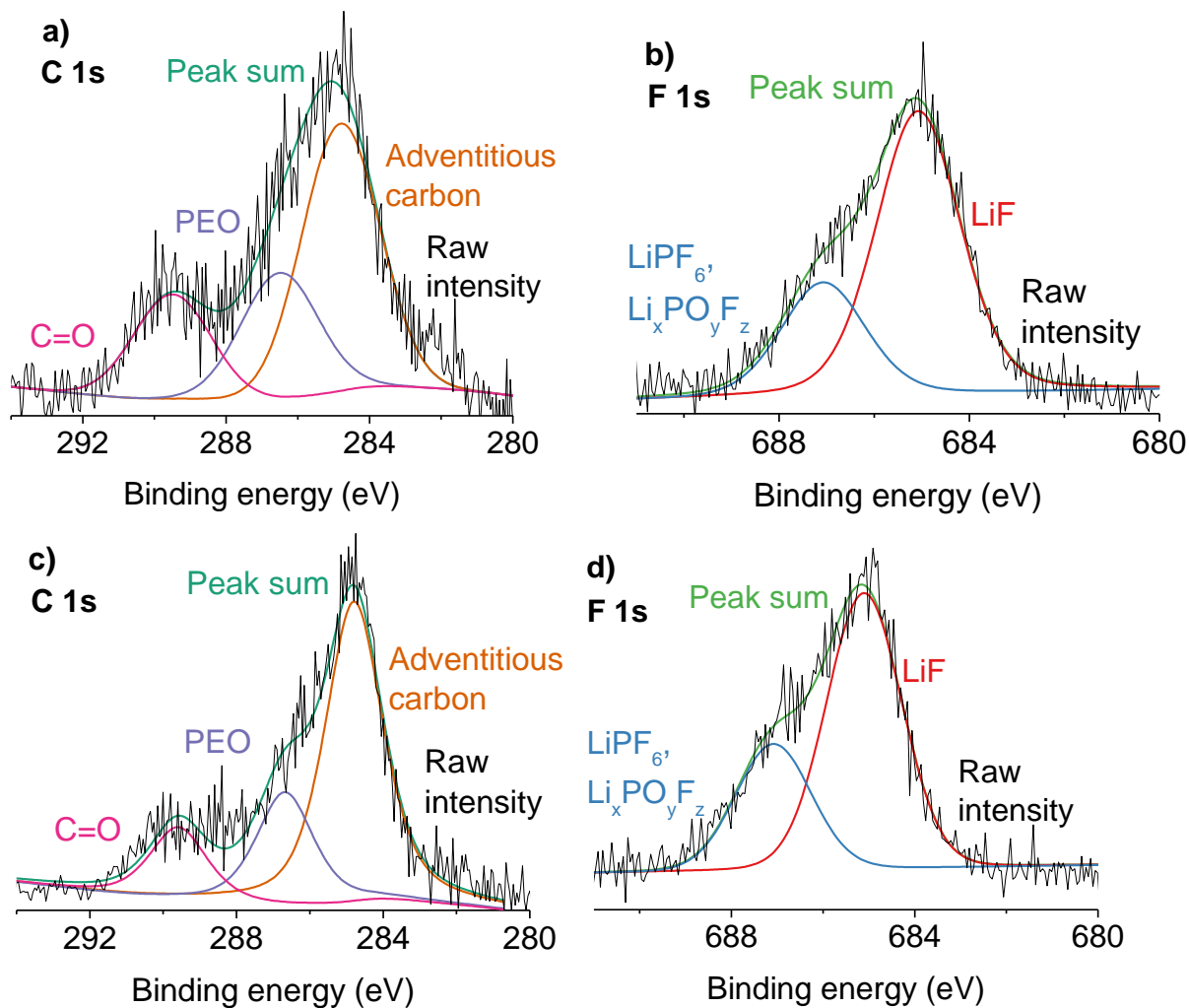


Figure S13. C1s (a, c) and F1s (b, d) XPS spectra of the Li electrode after 94 cycles in LP30 (a-b) and LP30 + 0.1 M KPF₆ (c-d).

Energy-dispersive X-ray spectroscopy

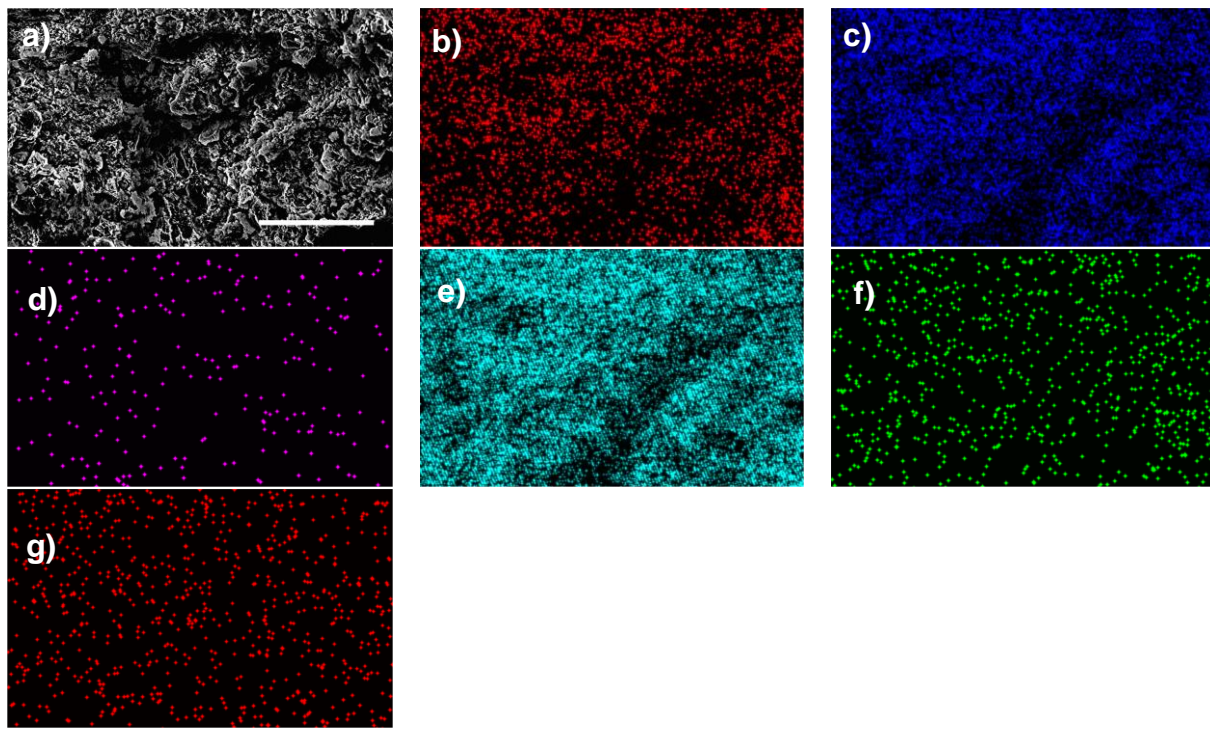


Figure S14. Cross-sectional SEM image of Li microstructure polarized in LP30 (a) and the corresponding EDS map for b) C K α_1 , b) F K α_1 , c) K K α_1 , d) O K α_1 , e) P K α_1 , and f) Si K α_1 . Scale bar = 7 μm .

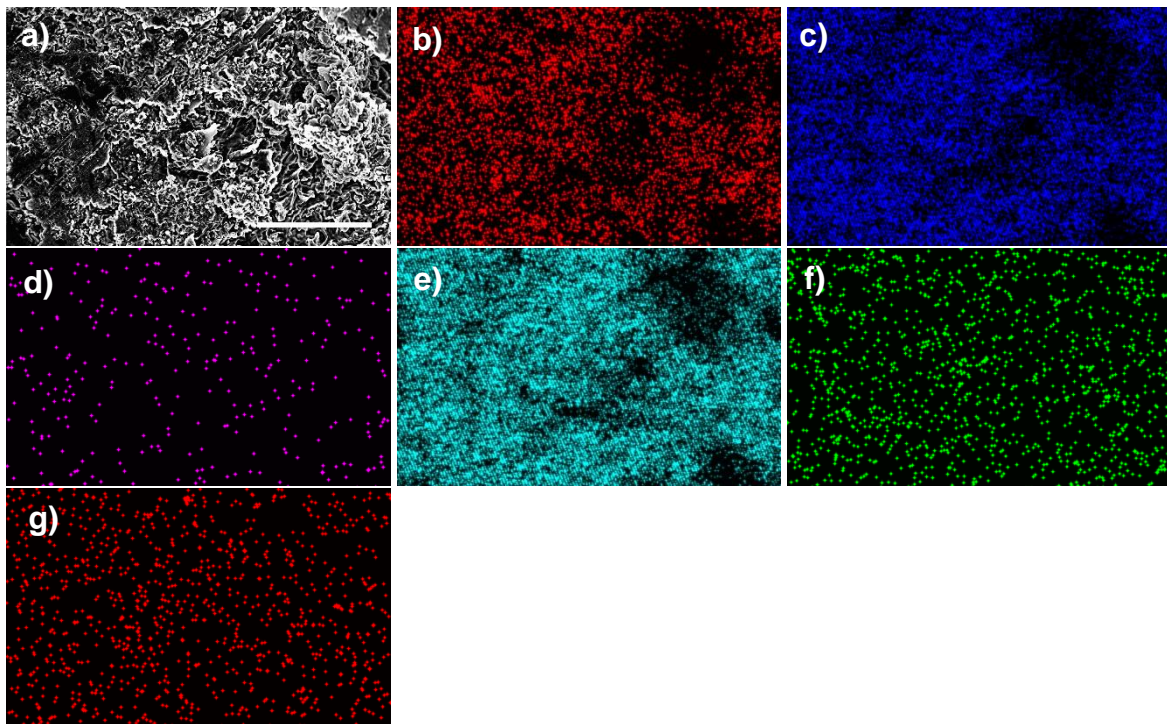


Figure S15. Cross-sectional SEM image of Li microstructure polarized in LP30 + 0.1 M KPF₆ (a) and the corresponding EDS map for b) C K α_1 , b) F K α_1 , c) K K α_1 , d) O K α_1 , e) P K α_1 , and f) Si K α_1 . Scale bar = 7 μm .

Comparing the EDS intensities of K with the Si background (leveraging the fact that Si is absent from the sample) yields similar K/Si intensity ratios for LP30 (30%) and LP30 + 0.1 M KPF₆ (27%), suggesting that K is not depositing in significant amounts on the surface of the electrode.

Atomic Absorption Spectroscopy

Table S2. Amount of KPF₆ lost after cycling as measured by AAS. Li/Li symmetric cells were cycled in LP30 + 0.1 M KPF₆, and the concentration of the electrolyte was measured using AAS before and after cycling to calculate % K lost after cycling.

| Number of Samples | Cycles | % K lost after cycling | Standard error |
|-------------------|--------|------------------------|----------------|
| 8 | 1 | 18.5% | 2.9% |
| 3 | 20 | 12.2% | 5.5% |
| 1 | 50 | 17.2% | 0.0% |
| 1 | 93 | 11.2% | 0.0% |

Karl Fischer Titration

Table S3. Water content of electrolytes as measured using a Karl Fischer titration (titration measurements provide ~20 ppm resolution).

| Electrolyte | Water content (ppm) |
|--------------------------------------|---------------------|
| LP30 | 9.3 |
| LP30 + 0.1 M LiPF₆ | 2.2 |
| LP30 + 0.1 M KPF₆ | 4.1 |

DFT

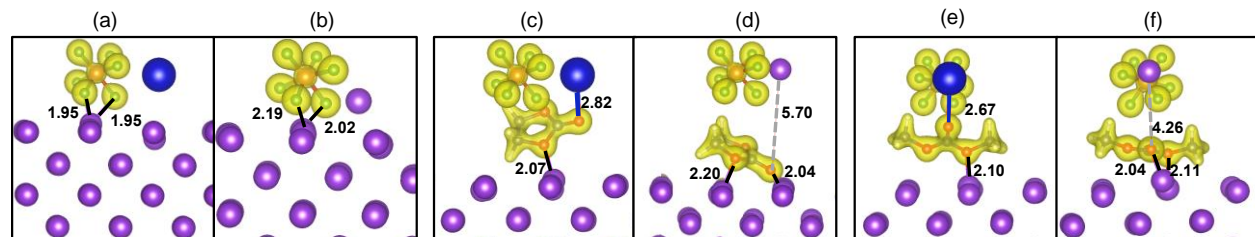


Figure S16. Electron density distributions (shown in yellow isosurfaces) of DFT-optimized Li metal-electrolyte interfacial geometries with KPF₆ and LiPF₆. The electron densities are found concentrated around PF₆⁻ anions in the case of a) KPF₆ + Li surface and b) LiPF₆ + Li surface, with most of the electron density surrounding the -F functional groups. For the cases involving EC and DMC, the electron densities are found concentrated around both PF₆⁻ anions and the solvent molecules as shown in c) KPF₆ + EC + Li surface, d) LiPF₆ + EC + Li surface, e) KPF₆ + DMC + Li surface and f) LiPF₆ + DMC + Li surface. For EC and DMC, most of the electron density is found around the singly bonded oxygen (-O-) and the carbonyl oxygen (=O) of the carbonate functional group. The electron density distributions demonstrate that bonds between the cations and the Li surfaces are formed through the most negatively charged functional groups, suggesting that solvent-salt coordination and electrolyte-surface interactions exhibit chemisorption characteristics.

Scanning Electron Microscopy

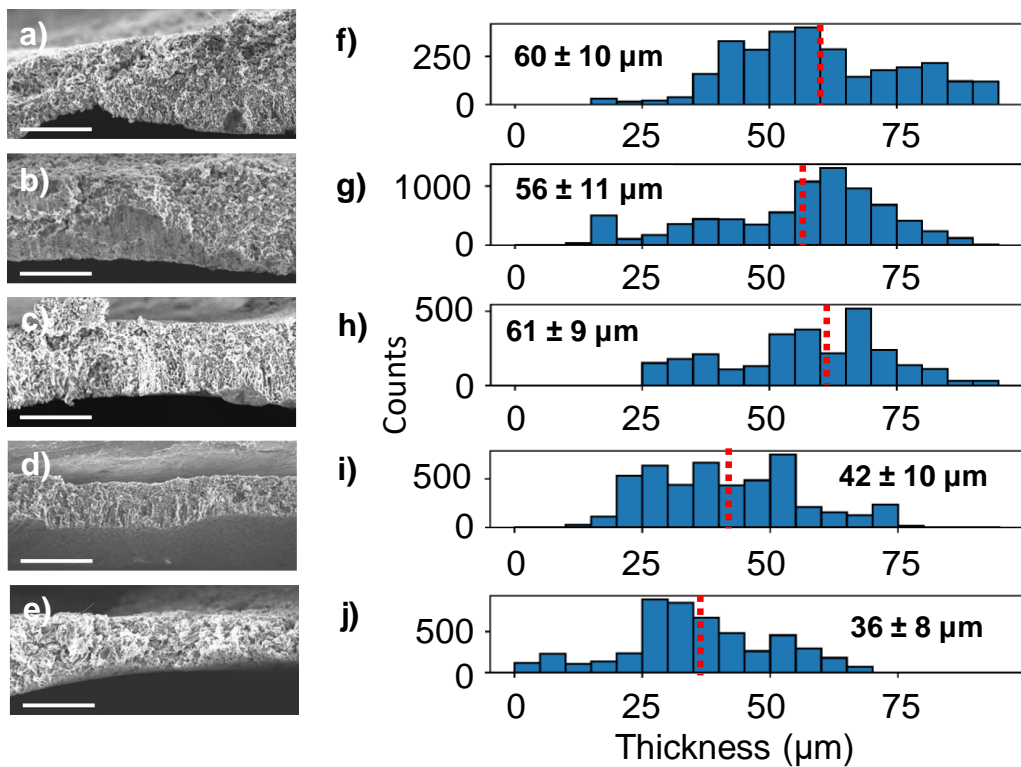


Figure S17. Representative images of Li microstructural thickness and histograms of microstructural thickness distributions of electrodeposited Li in a) LP30 electrolyte, b) LP30 + 0.1 M LiPF₆, c) LP30 + 0.1 M KPF₆, d) LP30 + 0.15 M KPF₆, and e) LP30 + 0.25 M KPF₆ after galvanostatic polarization at 1 mA cm^{-2} for 2 h.

Supplemental Experimental Procedures

Analysis of scanning electron micrographs

Each electrode sample was cut in half to produce two separate samples for analysis: one to probe the surface of the Li metal electrode exposed to the electrolyte (to evaluate microstructural morphology) and another for cross-sectional examination of the electrode (to measure microstructural thickness).

Cross-sectional SEMs were analyzed using ImageJ.³ Images were first rotated so the microstructural layer was vertically oriented, and the freehand line tool was used to record the coordinates of the edges of each microstructural layer. A Python script written in-house was used to measure the x-distance between the microstructural edges at each y-pixel and generate a microstructural thickness distribution for each electrolyte composition. Thicknesses were measured for 7-25 images of 2-3 samples for a total of 2500-8500 different pixel values for each electrolyte composition. Portions of the Li electrode lacking microstructural growth in Figure 1i-11 were neglected in the overall thickness distribution because these regions are randomly distributed and determined to be too difficult to accurately quantify.

Coulombic efficiency

Coulombic efficiency (CE) was measured using Li/Cu coin cells at a current density of 0.5 mA cm⁻². 0.5 mAh cm⁻² was deposited from the Li electrode onto the Cu substrate and then stripped for 100 cycles, with the stripping capacity:plating capacity ratio used to calculate CE for each cycle (Figure S2). Average CE and error bars representing standard error over three cells are plotted as a function of cycle number.

Solution NMR measurements

All solution NMR experiments were performed on a Bruker Avance III 400 spectrometer equipped with a triple resonance broadband observe (TBO) probehead. All spectra were recorded at room temperature (T = 295 K). One-dimensional (1D) ¹H (30° single pulse, 1 s recycle delay, 64 scans, internally referenced to residual DMSO at 2.5 ppm), ⁷Li (90° single pulse, 2 s recycle delay, 8 scans, externally referenced to 1 M aqueous LiCl at 0 ppm), ¹³C (30° single pulse with WALTZ-16 ¹H decoupling, 3 s recycle delay, 7168 scans, internally referenced to DMSO at 39.5 ppm), ¹⁹F (30° single pulse, 2 s recycle delay, 32 scans, internally referenced to PF₆⁻ at -72.4 ppm), and ³¹P (30° single pulse with WALTZ-16 ¹H decoupling, 1 s recycle delay, 128 scans, internally referenced to PF₆⁻ at -146 ppm) NMR spectra were recorded on pristine electrolyte samples as well as electrolyte extracted from Li/Li coin cells after cycling.

Two-dimensional (2D) heteronuclear single quantum correlation (HSQC) spectra were recorded using the ‘hsqcetgp’ Bruker pulse program, with 2D ¹H-¹³C correlation via double INEPT (insensitive nuclei enhanced polarization transfer). The acquisition was phase sensitive using Echo-Antiecho-TPPI gradient selection with ¹³C GARP decoupling during acquisition, using trim pulses. The direct dimension (¹H) was acquired with a time domain of 1024 points over a sweep width of 12 ppm and a transmitter frequency offset of 3.68 ppm. The indirect dimension (¹³C) was acquired using a time domain of 256 points over a sweep width of 200 ppm with a transmitter frequency offset of 100 ppm. The recycle delay was set to 1.5 s with 4 scans per slice.

2D heteronuclear multiple bond correlation (HMBC) spectra were recorded using the ‘hmbcgpl2ndqf’ Bruker pulse program, with 2D ^1H - ^{13}C correlation via heteronuclear zero and double quantum coherence. The acquisition was optimized on long-range couplings set to 8 Hz, with a two-fold low-pass J-filter to suppress one-bond correlations and no decoupling during the acquisition. The direct dimension (^1H) was acquired using a time domain of 2048 points over a sweep width of 10 ppm and a transmitter frequency offset of 3.68 ppm, and indirect dimension (^{13}C) was acquired using a time domain of 256 points over a sweep width of 220 ppm with a transmitter frequency offset of 100 ppm. The recycle delay was set to 1.5 s with 4 scans per slice.

Solid-state NMR measurements

All SSNMR experiments were performed on a Bruker Avance NEO 600 MHz spectrometer equipped with either a 3.2 mm HXY MAS Chemagnetics probehead or a 1.6 mm HXY MAS Chemagnetics probehead. All spectra were collected at room temperature. Prior to each measurement, the magic-angle was set using KBr. ^1H - ^{13}C cross polarization magic-angle spinning (CPMAS) measurements were performed with a Hartmann-Hahn match of 60 kHz with a ramped (70-100%) pulse on ^1H , a contact time of 5.5 ms, a recycle delay of 8 s, and between 27019 and 76800 scans. ^{13}C direct polarization experiments were collected using a spin-echo pulse sequence ($90^\circ - \tau - 180^\circ - \tau - \text{acquire}$, with $\tau = 96.5 \mu\text{s}$), ^1H TPPM decoupling at 125 kHz, a recycle delay of 30 s, and 2864 scans. ^{19}F SSNMR experiments were performed using a spin-echo pulse sequence ($\tau = 95.7 \mu\text{s}$), a recycle delay of 30 s recycle delay, and 2731 scans. ^1H NMR was externally referenced to adamantane at 1.8 ppm, ^{13}C NMR was externally referenced to adamantane at 38.5 ppm, and ^{19}F was externally referenced to LiF at -204 ppm.

^1H -detected ^1H - ^{13}C heteronuclear correlation (HETCOR) experiments⁷⁰ were performed at a magic-angle spinning (MAS) frequency of 27 kHz and a ^1H radiofrequency (rf) power of 100 kHz. Forward ^1H - ^{13}C CP was achieved with a ramped pulse on ^1H (70-100%, contact time of 3 ms) and magnetization was transferred back from ^{13}C to ^1H after t_1 evolution using backward CP (ramped pulse 100-70%, contact time of 1 ms) for ^1H detection. Background ^1H magnetization was removed using two saturation blocks consisting of a 90° pulse followed by a set of 400 μs spin-lock pulses at the HORROR condition and a 10 ms dephasing delay. ^1H decoupling using SPINAL-64 at 125 kHz was applied during t_1 evolution periods.

X-ray photoelectron spectroscopy

Li/Li symmetric coin cells were galvanostatically cycled using Celgard separators at 1 mA cm⁻² for 2 h charge/discharge cycles. Li electrodes were removed from the cell and dipped in DMC for 1 min to remove residual salts and prevent charging in the XPS. Samples were dried *in vacuo* overnight to remove residual electrolyte solvent and prevent sample off-gassing in the evacuated XPS chamber. The samples were mounted on XPS stubs inside of the glovebox using carbon tape. Samples were transferred to the XPS sample chamber using an airtight Ar-filled jar, with exposure to atmosphere estimated to be <5 s for each sample. Spectra were collected using a PHI 5600 XPS system with a hemispherical analyzer and an Al X-ray source with XPS base chamber pressure $< 3.5 \times 10^{-9}$ Torr. XPS Peak 41 software was used to fit spectra, providing both peak locations and integrations. The adventitious carbon peak in the C 1s spectrum was used to reference to 284.8 eV. Peaks were assigned to PEO (C 1s, ~286.5 eV), C=O (C 1s, ~289-290

eV), LiF (~684-685 eV), and $\text{Li}_x\text{PO}_y\text{F}_z$ (F 1s, ~287-288 eV).¹ All peaks were fit using a Shirley baseline correction, with two constraints: i) the Gaussian:Lorentzian ratio was the same for all peaks in a given orbital, and ii) the full width at half maximum (fwhm) was the same for all peaks in a given orbital. Peak areas were normalized by atomic sensitivity factors to determine the relative product composition on each Li metal electrode.

Atomic absorption spectroscopy (AAS)

A flooded cell was machined in-house from PTFE to exhibit a 1 cm active diameter and a 1 cm spacing between electrodes. No separator is required in the cell. Electrolyte samples were prepared by cycling Li/Li symmetric cells in the PTFE flooded cell (1, 20, 50, and 93 cycles for 2 h at 1 mA cm⁻², Table S2). Electrolyte extracted from flooded cells was filtered using a PTFE syringe filter with 200 nm pore size to remove Li particles. 2.5 μL of electrolyte (both pristine and cycled) was dried *in vacuo* overnight to remove organic solvent, then diluted to 10 mL in 10 mL volumetric flasks, using 1000 ppm Cs AAS standard to eliminate ionization interference.² Standard concentrations (0.1, 0.5, 1, 2, 3 ppm K) were prepared to construct a calibration curve with 1.8 ppm Li (the equivalent of 1 M Li in the electrolyte after dilution for AAS) and 1000 ppm Cs in a 2% (v/v) HNO₃ matrix using commercially available AAS standards. Pristine and cycled samples were analyzed using an iCE 3300 AAS (Thermo Fisher Scientific Ltd) equipped with a 50 mm burner and fit to a quadratic absorption-concentration relationship obtained from the calibration curves.

Calculation of Bader Charge Transfers

Bader analysis is an approach to determine the electronic charges on individual atoms in molecules or crystals. The partitions of the atom boundaries are based on an electronic zero-flux surface (i.e. a 2-D surface on which the charge density is at a minimum perpendicular to the surface). Naturally, this surface determines the separation between two atoms in a bonding environment. For the prior in Bader analysis, a “.cube” file containing electron density as a function of spatial coordination of the final optimized DFT geometry is produced. This file is then used to calculate the charges on each atom in the optimized system. The Bader charge transfers are calculated by comparing the initial atomic charges and the Bader charges of the Li surface slabs. The overall simulated geometries are charge-neutral before and after Bader analysis.

Supplementary References

1. Eshetu, G.G., Diemant, T., Grugeon, S., Behm, R.J., Laruelle, S., Armand, M., and Passerini, S. (2016). In-Depth Interfacial Chemistry and Reactivity Focused Investigation of Lithium-Imide- and Lithium-Imidazole-Based Electrolytes. *ACS Appl. Mater. Interfaces* 8, 16087–16100.
2. Karpiuk, U.V., Mohammad, K., Azzam, A., Helmi, Z., and Abudayeh, M. (2016). Qualitative and Quantitative Content Determination of Macro - Minor Elements in *Bryonia Alba L.* Roots using Flame Atomic Absorption Spectroscopy Technique. *Tabriz Univ. Med. Sci.* 6, 285–291.